

Spreading and multi-wavelength emissions of an ultra-narrow relativistic jet from GRB 221009A

JIN-JUN GENG,¹ YING-KANG ZHANG,^{2,3} HAO-XUAN GAO,¹ FAN XU,⁴ BING LI,^{5,6} TIAN-RUI SUN,¹ AI-LING WANG,^{2,7}
ZHI-JUN XU,² YUAN-QI LIU,² JUN YANG,⁸ CHEN-RAN HU,⁴ LAUREN RHODES,^{9,10} LIANG LI,^{11,12} YU WANG,¹³ YE LI,¹
DI XIAO,¹ JIA REN,⁴ BING ZHANG,^{14,15} TAO AN,^{2,3,*} XUE-FENG WU,^{1,16,†} YONG-FENG HUANG,^{4,17,‡} AND ZI-GAO DAI^{16,§}

¹*Purple Mountain Observatory, Chinese Academy of Sciences, Nanjing 210023, P. R. China*

²*Shanghai Astronomical Observatory, Chinese Academy of Sciences, 80 Nandan Road, Shanghai 200030, P. R. China*

³*Key Laboratory of Radio Astronomy and Technology, Chinese Academy of Sciences, A20 Datun Road, Beijing 100101, P. R. China*

⁴*School of Astronomy and Space Science, Nanjing University, Nanjing 210023, P. R. China*

⁵*Key Laboratory of Particle Astrophysics, Institute of High Energy Physics, Chinese Academy of Sciences, Beijing 100049, P. R. China*

⁶*Guangxi Key Laboratory for Relativistic Astrophysics, Nanning 530004, P. R. China*

⁷*School of Astronomy and Space Science, University of Chinese Academy of Sciences, Beijing 100049, P. R. China*

⁸*Department of Space, Earth and Environment, Chalmers University of Technology, Onsala Space Observatory, SE-439 92 Onsala, Sweden*

⁹*Trottier Space Institute at McGill, 3550 Rue University, Montreal, Quebec H3A 2A7, Canada*

¹⁰*Department of Physics, McGill University, 3600 Rue University, Montreal, Quebec H3A 2T8, Canada*

¹¹*Institute of Fundamental Physics and Quantum Technology, Ningbo University, Ningbo, Zhejiang 315211, P. R. China*

¹²*Department of Physics, School of Physical Science and Technology, Ningbo University, Ningbo, Zhejiang 315211, P. R. China*

¹³*ICRANet, Piazza della Repubblica 10, I-65122 Pescara, Italy*

¹⁴*Nevada Center for Astrophysics, University of Nevada, Las Vegas, NV 89154, USA*

¹⁵*Department of Physics and Astronomy, University of Nevada, Las Vegas, NV 89154, USA*

¹⁶*School of Astronomy and Space Sciences, University of Science and Technology of China, Hefei 230026, P. R. China*

¹⁷*Key Laboratory of Modern Astronomy and Astrophysics (Nanjing University), Ministry of Education, Nanjing 210023, P. R. China*

ABSTRACT

The long-term evolution of relativistic jets in gamma-ray bursts (GRBs), particularly from days to months post-burst, remains a fundamental puzzle in astrophysics. Here, we report our very long baseline interferometry observation of the brightest GRB 221009A from 5 to 26 days post-burst. Combined with released data, we uncover a remarkable two-stage evolution of the jet lateral size. The jet size initially grew slowly but later expanded rapidly, challenging conventional scenarios. The slow-evolving stage provides a robust lower limit on the jet opening angle and direct evidence of jet propagation in the uniform interstellar medium at this period. The synergy analysis of the whole jet size evolution and multi-wavelength emissions uncovers that GRB 221009A harbors an ultra-narrow jet (with a half-opening angle $\simeq 0.01\text{-}0.03$ radian) that propagates through a wind-like medium before encountering the interstellar medium, which finally undergoes lateral spreading after significant deceleration. These findings provide crucial new insights into relativistic jet dynamics and establish GRB 221009A as a unique case study for understanding the complex physics of GRB outflows.

1. INTRODUCTION

Gamma-ray bursts (GRBs) are flashes of gamma rays arising from cataclysmic cosmic events. A fundamental aspect of GRB physics is the relativistic jet that powers these explosions (Kumar & Zhang 2015). The GRB outflow has traditionally been modeled as a conical jet with a half-opening angle of the order of 0.1 radians, supported by observations of a steepening break in their afterglow lightcurves (“jet break”). While early models assumed a simple uniform structure, an angle-dependent structured jet (Mészáros et al. 1998; Dai & Gou 2001; Rossi et al. 2002; Zhang & Mészáros 2002; Kumar & Granot 2003) may better represent the true nature of these outflows, as demonstrated in some GRBs including the gravitational-wave-associated short GRB 170817A (Lamb & Kobayashi 2017; Troja et al.

* E-mail: antao@shao.ac.cn

† E-mail: xfwu@pmo.ac.cn

‡ E-mail: hyf@nju.edu.cn

§ E-mail: daizg@ustc.edu.cn

2017; Granot et al. 2017; Lazzati et al. 2018; Kathirgamaraju et al. 2018; Gottlieb et al. 2018; Troja et al. 2019; Ryan et al. 2020). Very long baseline interferometry (VLBI) is the most powerful tool to directly image nearby GRB jets and study their complex geometry and dynamics. The successful size measurements and proper motion detection in GRB 030329 (Taylor et al. 2004, 2005; Pihlström et al. 2007) and GRB 170817A (Ghirlanda et al. 2019; Mooley et al. 2018, 2022) have provided crucial clues to unveil the nature of those jets.

GRB 221009A, discovered on 2022 October 9, is the record holder as the brightest GRB ever detected, with isotropic equivalent energy exceeding 10^{55} erg (Lesage et al. 2023; An et al. 2023; LHAASO Collaboration et al. 2023; Burns et al. 2023; Frederiks et al. 2023). Its energy level and relative proximity ($z = 0.151$ (de Ugarte Postigo et al. 2022; Castro-Tirado et al. 2022)) make GRB 221009A an ideal natural laboratory for detailed multi-wavelength investigations. The extensive follow-up campaigns have revealed its temporal and spectral evolution across the electromagnetic spectrum. Starting as early as the prompt stage, the tera-electron volt (TeV) emission was detected by the Large High Altitude Air Shower Observatory (LHAASO) Collaboration (LHAASO Collaboration et al. 2023). Sustained emissions are recorded in the TeV, GeV, X-ray, optical, and radio bands (LHAASO Collaboration et al. 2023; Axelsson et al. 2024; Williams et al. 2023; Ravasio et al. 2024; O’Connor et al. 2023; Laskar et al. 2023; Levan et al. 2023; Bright et al. 2023; Rhodes et al. 2024), providing a rich dataset to probe the jet properties. Recently acquired high-resolution imaging through VLBI has added a crucial new dimension to our understanding of this exceptional event (Giarratana et al. 2024). Several models have been proposed to interpret the multi-wavelength emission of GRB 221009A, invoking non-uniform jet structures (Gill & Granot 2023; Sato et al. 2023; O’Connor et al. 2023; Ren et al. 2024; Zhang et al. 2024; Zheng et al. 2024), specific burst environments (Ren et al. 2023; Zheng et al. 2024), multiple emission components (Isravel et al. 2023; Zhang et al. 2023), and evolving microphysics shock parameters (Frajia et al. 2024; Foffano et al. 2024). Despite the wealth of observational data gathered on GRB 221009A, a coherent physical picture of GRB 221009A remains elusive, particularly when considering the complex details revealed by VLBI observations.

The published VLBI observations utilizing the European VLBI Network (EVN) and the Very Long Baseline Array (VLBA) manifest the expansion of the relativistic jet of GRB 221009A (Giarratana et al. 2024). However, these observations are limited to 40-262 days post-burst (Giarratana et al. 2024), leaving a gap in understanding the earliest jet evolution. This gap is particularly significant because the simple extrapolation of the size evolution by VLBA would result in a relatively large jet opening angle at a potential jet break time of ~ 0.8 days (O’Connor et al. 2023) (Appendix), which appears inconsistent with other observational evidence. Therefore, the early-time VLBI observations are crucial for constructing a complete picture of the jet dynamics.

2. RESULTS

Here, we present the VLBI data observed in the first month, from 5 to 26 days post-burst (Table 1). Our analyses uncover important clues regarding the geometry, motion, and evolving nature of the outflow, which are crucial for developing credible models of this peculiar GRB. Throughout our VLBA observation campaign, GRB 221009A maintained its appearance as a compact radio source (see Fig. 1). The lack of substantial centroid shift suggests an on-axis jet aligned with our line of sight. When compared with GRB 030329 at a similar distance, the lateral size of GRB 221009A is significantly larger, consistent with its extremely energetic nature. By incorporating the VLBI data at the same frequency (15 GHz) observed 40 days after the burst (Giarratana et al. 2024), we find that the source size evolution is better described by a broken power-law (Fig. 2) than a single power-law according to the reduced chi-square statistics (Appendix). It strongly supports the presence of two distinct evolutionary phases in the jet’s expansion. The observed size initially increased slowly as $\propto t_{\text{obs}}^{0.12}$ during the first month after the burst. After 120 days, the size grew more quickly as $\propto t_{\text{obs}}^{2.19}$. Among the rare three bursts with successful VLBI monitoring in the history, such a two-stage size evolution feature is observed for the first time, demonstrating the uniqueness of this jet and further challenging our understanding of the already very complex behavior of GRB 221009A.

The commonly discussed GRB jet structures include uniform top-hat jets, structured jets, and two-component jets (Extended Data Figure 1 and Appendix). We first consider a relativistic top-hat jet with an initial half-opening angle of $\theta_{j,0}$ propagating into a circumburst medium with a power-law profile of $\propto R^{-s}$, where R is the distance from the explosion center, and $s = 0$ and $s = 2$ correspond to a uniform interstellar medium (ISM) and a free stellar wind, respectively. A jet with an initial bulk Lorentz factor Γ_0 (typically > 100) gets decelerated when enough mass from the medium is shocked, typically in 100s of seconds. After the deceleration time, the jet dynamics well obeys the Blandford-McKee (BM) solution (Blandford & McKee 1976), i.e., the radius R increases with time as $t_{\text{obs}}^{1/(4-s)}$ and the Lorentz factor Γ decreases with time as $t_{\text{obs}}^{(s-3)/(8-2s)}$. Beyond the jet break time, an on-axis observer would observe a

projected jet angular size as $\Phi = 2R \sin(\theta_{j,0})/D_A \propto t_{\text{obs}}^{1/(4-s)}$, where D_A is the cosmological angular diameter distance. Our analysis shows that the resulting evolution law of size in the ISM case, $\Phi \propto t_{\text{obs}}^{0.25}$, is more consistent with the slow-evolving stage than that in the wind case, $\Phi \propto t_{\text{obs}}^{0.5}$ (Extended Data Figure 2), which is also supported by the spectroscopic James Webb Space Telescope (JWST) observations (Blanchard et al. 2024) (see Appendix). Furthermore, our early size data sets a robust lower limit of $\theta_{j,0} \geq 0.01$ rad (Appendix). However, both cases fail to account for the fast-evolving stage observed at late times.

We next examine structured jet scenarios. The realistic jet may be structured, usually with a quasi-uniform core and an outer wing with reducing isotropic-equivalent energy and Lorentz factor as a function of angle, shaped either by the launching process of the central engine or interactions between the jet and the stellar envelope of the progenitor (Tchekhovskoy et al. 2008; Bromberg et al. 2011). If the initial Lorentz factor Γ_{edge} and the angle θ_{edge} of the wing edge satisfies $\Gamma_{\text{edge}} > 1/\theta_{\text{edge}}$, the observed source size could in principle be defined by the boundary at which when emission of the structured jet at a given latitude enters the field of view. The size increases during the gradual deceleration of the jet. For the jet wing with a conventional power-law energy profile, i.e., $E_{K,\text{iso}} \propto \theta^{-k_E}$, the predicted size evolution is $\Phi \propto t_{\text{obs}}^{(5-k_E)/(8-k_E)}$ for $s = 0$ and $\Phi \propto t_{\text{obs}}^{(3-k_E)/(4-k_E)}$ for $s = 2$. However, our analysis reveals that no reasonable values for k_E could be found to interpret both the early slow-evolving stage and the late fast-evolving stage of GRB 221009A (Appendix).

A third theoretical possibility emerges from models suggesting that a relativistic jet would retain its initial opening angle in the ultrarelativistic phase, but would enter a fast lateral expansion phase later, where the jet opening angle grows with radius, asymptotically reaching an exponential growth phase (Rhoads 1999; Granot & Piran 2012). The lateral expansion could in principle explain the observed fast-evolving stage, both for the ISM and the wind cases. For very narrow jets, e.g., $\theta_{j,0} \ll 10^{-1.5} \approx 0.03$ (Granot & Piran 2012), it may spread significantly when $\Gamma \approx \zeta/\theta_{j,0}$. In this context, the highly uncertain dimensionless parameter ζ (< 1), is constrained to be less than 0.5 from our observations. Adding to this picture, the temporal break of X-ray/optical afterglows (O'Connor et al. 2023) also hints at an upper limit of $\theta_{j,0} \leq 0.03$ rad. Therefore, the joint analyses of our VLBI observation, the afterglow properties, and the spectroscopic observations of JWST (Blanchard et al. 2024) suggest the intriguing dynamic evolution of a relativistic jet with an initial narrow half-opening angle of $\theta_{j,0} \in [0.01, 0.03]$ rad, which is characterized by the jet break, environment change, and lateral spreading (Appendix).

An alternative explanation for the observed fast-evolving stage could involve the emergence of a new emission component at late times. Such a component could arise either angularly from larger latitudes or radially from slower ejecta with lower Lorentz factors or a later injection time. However, both scenarios require unconventional parameters to interpret the late rapid expansion phase (Appendix). Another plausible explanation is a transition from reverse shock to external shock dominance. Nevertheless, the modeling of afterglow lightcurves (Fig. 3) indicates that such emission transition is expected to occur within 3×10^5 s at 15 GHz, significantly earlier than the observed size transition at 10^7 s (Fig. 4), and the corresponding size of the reverse shock would be considerably smaller than the observed size of the leading external shock.

The insights gained from the analysis of the jet dynamics inspire us to delve into understanding the complex multi-wavelength properties of GRB 221009A. The multi-pulse feature of the prompt emission and the synergy analysis of multi-wavelength afterglow orient us to propose the two-shell collision scenario (Appendix), in which the early TeV emission comes from the forward shock generated during the interaction between the preceding shell and a fast shell launched later. The reverse shock propagating into the fast shell contributes to the observed early radio emissions, while the forward shock turns into an external shock after crossing the preceding shell and produces long-lasting multi-wavelength afterglows (Extended Data Figure 4). With detailed numerical calculations, our scenario successfully interprets both the multi-wavelength data and the size evolution of GRB 221009A (Fig. 3 and Fig. 4). Early high-cadence radio observations of GRB 221009A help further constrain the magnetization of the fast shell to be of the order of 10^{-3} , which means the original outflow should be at least moderately magnetized, consistent with the magnetic reconnection origin of the prompt emission (Zhang & Yan 2011).

3. CONCLUSIONS

Our high-resolution VLBI monitoring, the argument of angle-corrected burst energy (Lesage et al. 2023), and the temporal behaviours of lightcurves (O'Connor et al. 2023) all converge to suggest that the jet of GRB 221009A possesses a narrow opening angle $\in [0.01, 0.03]$ rad. Although the concept of GRB jet spreading has long been theorized (Rhoads 1999; Granot & Piran 2012), it has remained observationally unverified due to the scarcity of direct

size measurements (Taylor et al. 2004; Ghirlanda et al. 2019). The likelihood of observing such a narrowly collimated jet on-axis is exceedingly low, further complicating direct detection. Our observations provide the first evidence of jet spreading and its underlying physical condition, thereby advancing the understanding of the origin of the complex multi-wavelength emission observed in GRB 221009A. Continued VLBI observations of this remarkable burst would validate this evolutionary scenario.

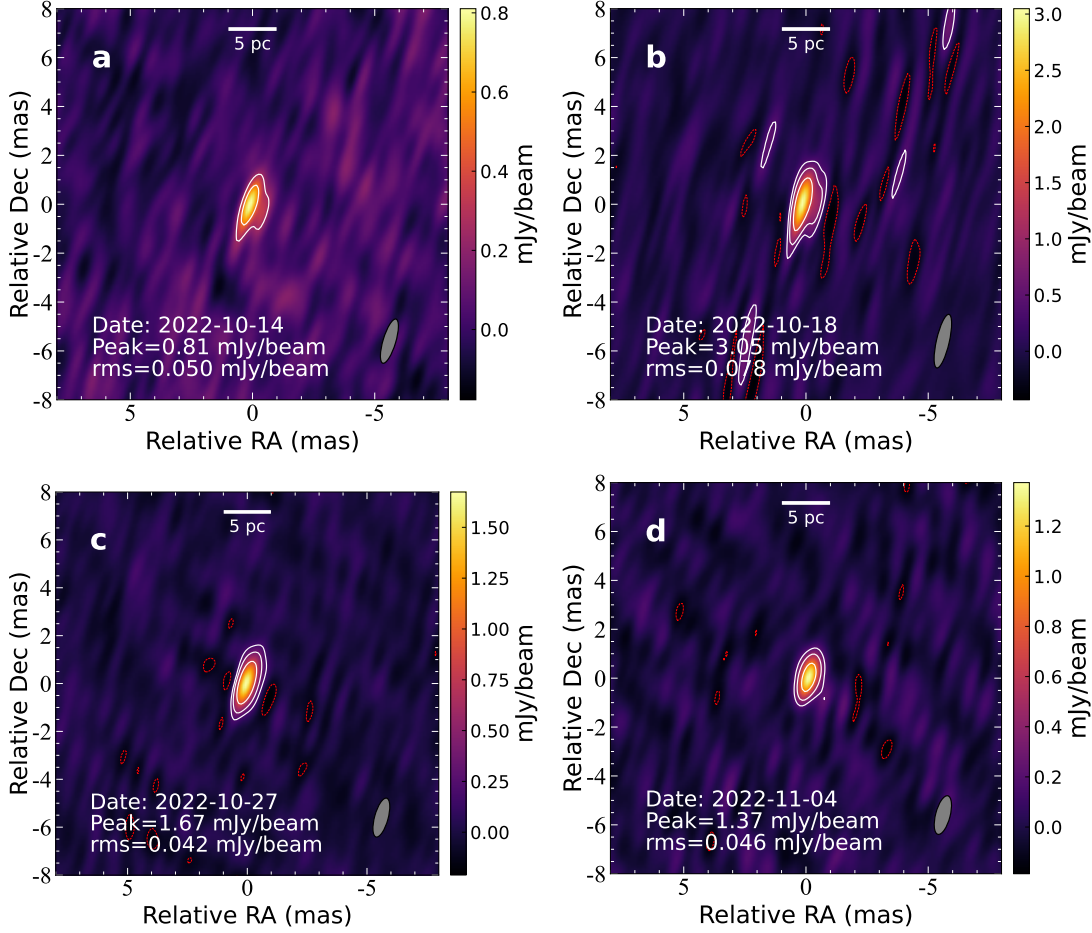


Fig. 1. VLBI images of GRB 221009A at 15 GHz. The observed four epochs are: 5 (a), 10 (b), 19 (c), 26 (d) days after burst. The observation date, peak intensity, and rms noise level are shown in each map. The observation information is listed in Extended Data Table 1. The beam shape is shown at the bottom right as a grey ellipse in each image. The image center has been shifted to the brightness peak (RA=19:13:03.501, DEC=+19:46:24.229).

Table 1. Parameters of GRB 221009A obtained from Difmap and MCMC model fitting.

| Code | (RA, Dec) (J2000) | Beam (mas × mas, °) | noise (mJy b ⁻¹) | S_{peak} (mJy b ⁻¹) | $S_{\text{total}}^{\text{difmap}}$ (mJy) | $S_{\text{total}}^{\text{mcmc}}$ (mJy) | θ^{difmap} (mas) | θ^{mcmc} (mas) | log T_{B} (K) |
|--------|-------------------------------|-------------------------|---------------------------------|---|---|---|-----------------------------------|---------------------------------|---------------------------|
| (1) | (2) | (3) | (4) | (5) | (6) | (7) | (8) | (9) | (10) |
| tg015 | 19:13:03.50080, 19:46:24.2289 | $1.9 \times 0.5, -16.7$ | 0.048 | 0.81* | 0.91 ± 0.06 | 0.91 ± 0.05 | 0.24 ± 0.06 | 0.24 ± 0.07 | 7.96 |
| ba161a | 19:13:03.50081, 19:46:24.2290 | $2.3 \times 0.5, -12.9$ | 0.078 | 3.05 | 3.46 ± 0.21 | 3.46 ± 0.07 | 0.27 ± 0.02 | 0.27 ± 0.02 | 8.46 |
| ba161b | 19:13:03.50081, 19:46:24.2289 | $1.7 \times 0.6, -15.4$ | 0.042 | 1.67 | 1.96 ± 0.05 | 1.96 ± 0.05 | 0.32 ± 0.02 | 0.32 ± 0.02 | 8.07 |
| ba161c | 19:13:03.50082, 19:46:24.2291 | $1.6 \times 0.6, -14.6$ | 0.046 | 1.37 | 1.56 ± 0.05 | 1.56 ± 0.06 | 0.30 ± 0.03 | 0.30 ± 0.04 | 8.02 |

Notes: * Due to the significant offset between the pointing center and the actual position of GRB 221009A in the test observation tg015, there are larger uncertainties in the total flux density and size measurements. Col. 1 – project code; Col. 2 – right ascension and declination coordinates; Col. 3 – the major axis, minor axis and position angle (from north to east) of the synthesized beam; Col. 4 – rms noise of the image; Col. 5 – peak flux density of the image; Col. 6 – total flux density fitted in DIFMAP; Col. 7 – total flux density derived from MCMC fit; Col. 8 – source size estimated from the VLBI resolution and image parameters; Col. 9 – source size from the MCMC fit; Col. 10 – brightness temperature of the VLBI component. Because the fitted component size is an upper limit, the resulting brightness temperature represents a lower limit.

REFERENCES

- Ai, S., & Zhang, B. 2021, MNRAS, 507, 1788
- An, T., Wu, X., Lao, B., et al. 2022, Sci. China. Phys. Mech. Astron., 65, 129501
- An, T., Wu, X.-P., & Hong, X. 2019, Nature Astronomy, 3, 1030
- An, Z.-H., Antier, S., Bi, X.-Z., et al. 2023, arXiv e-prints, arXiv:2303.01203

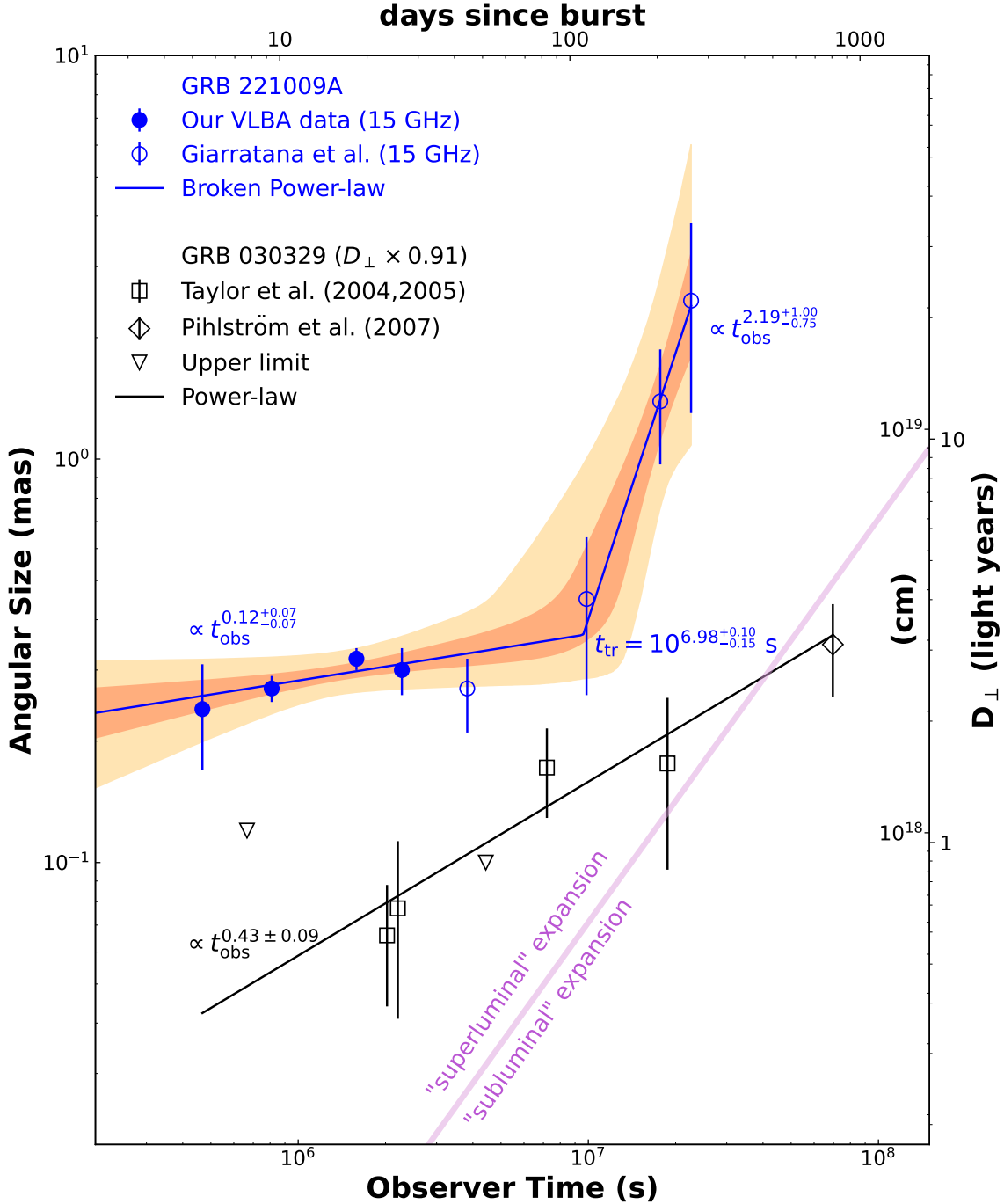


Fig. 2. Evolution of the source size over observer time. The blue solid line shows the size (angular diameter of D_{\perp}) evolution of GRB 221009A ($z = 0.151$) described by a broken power-law. The early slow stage evolves as $t_{\text{obs}}^{0.12 \pm 0.07}$ and the late fast-evolving stage as $t_{\text{obs}}^{2.19^{+1.00}_{-0.75}}$, separated by a transition time of $t_{\text{tr}} = 10^{6.98 \pm 0.15} \text{ s}$, where the error is given at the 1σ confidence. The 1σ and 3σ confidence intervals for the fit are shown by the deep orange and light orange shaded area, respectively. The blue filled circles represent the source sizes derived from our observational data, and the hollow circles indicate the sizes obtained from Giarratana et al. (2024). Note that the last point is derived by reprocessing the data as only an upper limit is given in Giarratana et al. (2024) (see Appendix). As a comparison, the size evolution of GRB 030329 (Taylor et al. 2004, 2005; Pihlström et al. 2007) at a comparable redshift of $z = 0.169$ is shifted to the same distance and shown with black squares and diamonds and fitted with a single power-law (black solid line), with a temporal index of 0.43 ± 0.09 at the 1σ confidence. The apparently superluminal motion is defined by $D_{\perp} > 2ct_{\text{obs}}$, on the upper left side of the purple line.

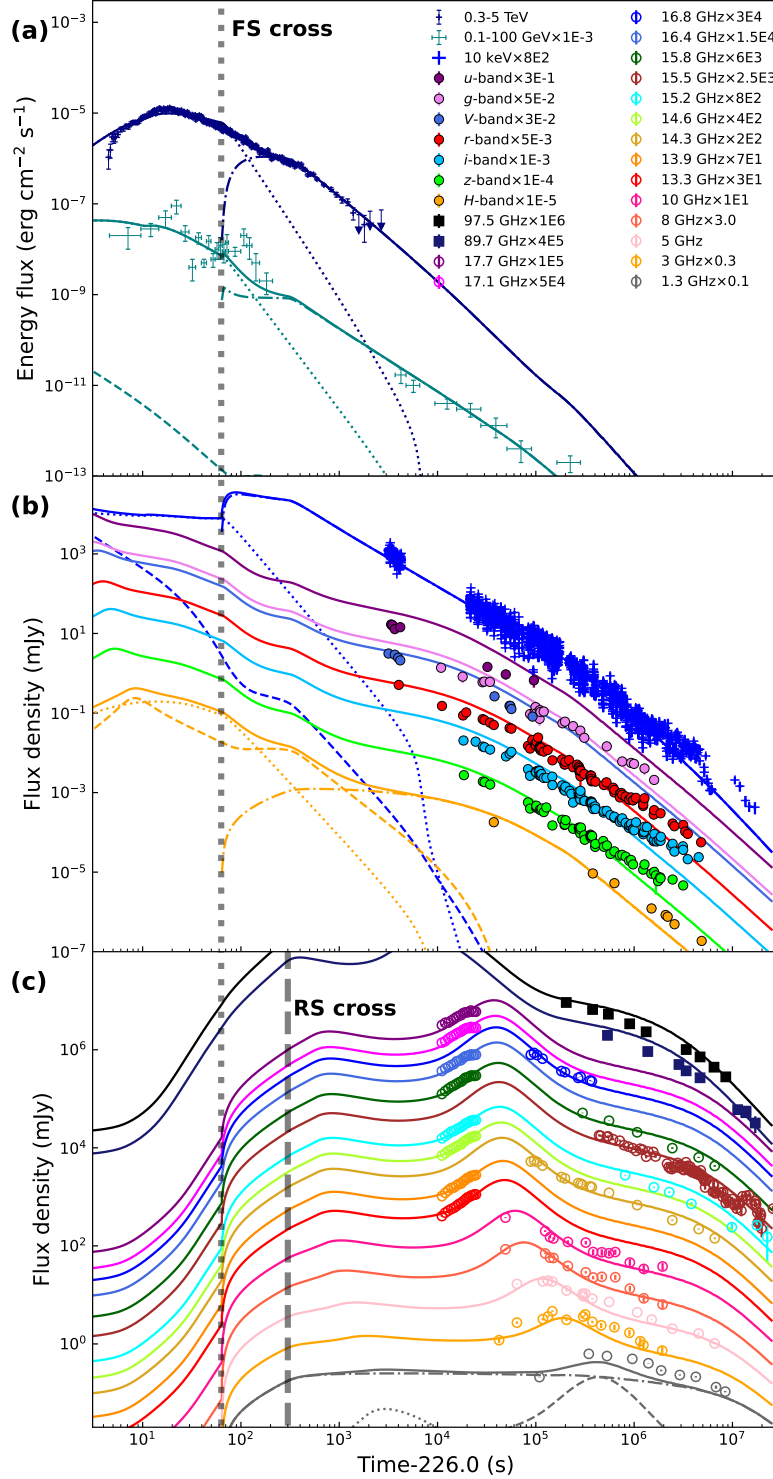


Fig. 3. Fit to the multi-wavelength lightcurves of GRB 221009A. Panels (a-c) show our numerical fitting to emissions in the high-energy bands (TeV and GeV), the X-ray and optical bands, and the low frequencies. In each panel, the dotted and dashed lines represent forward and reverse shock emission arising from the slow and fast outflow collision, respectively (Appendix). The dash-dotted lines are emissions of the external shock propagating in the surrounding medium. Solid lines are the sum of these components. The grey vertical dotted and dashed line mark the time that the forward shock (FS) and reverse shock (RS) crosses respectively. All the data of different frequencies, including the TeV range (LHAASO Collaboration et al. 2023), the GeV range (Axelsson et al. 2024), the optical bands (O’Connor et al. 2023; Laskar et al. 2023; Levan et al. 2023; Williams et al. 2023), and the radio bands (Laskar et al. 2023; Bright et al. 2023; Rhodes et al. 2024) are taken from the literature. The optical data have been only corrected for Galactic extinction of $E(B - V) = 1.32$ mag (Schlafly & Finkbeiner 2011), and the potential contribution from supernova is not subtracted.

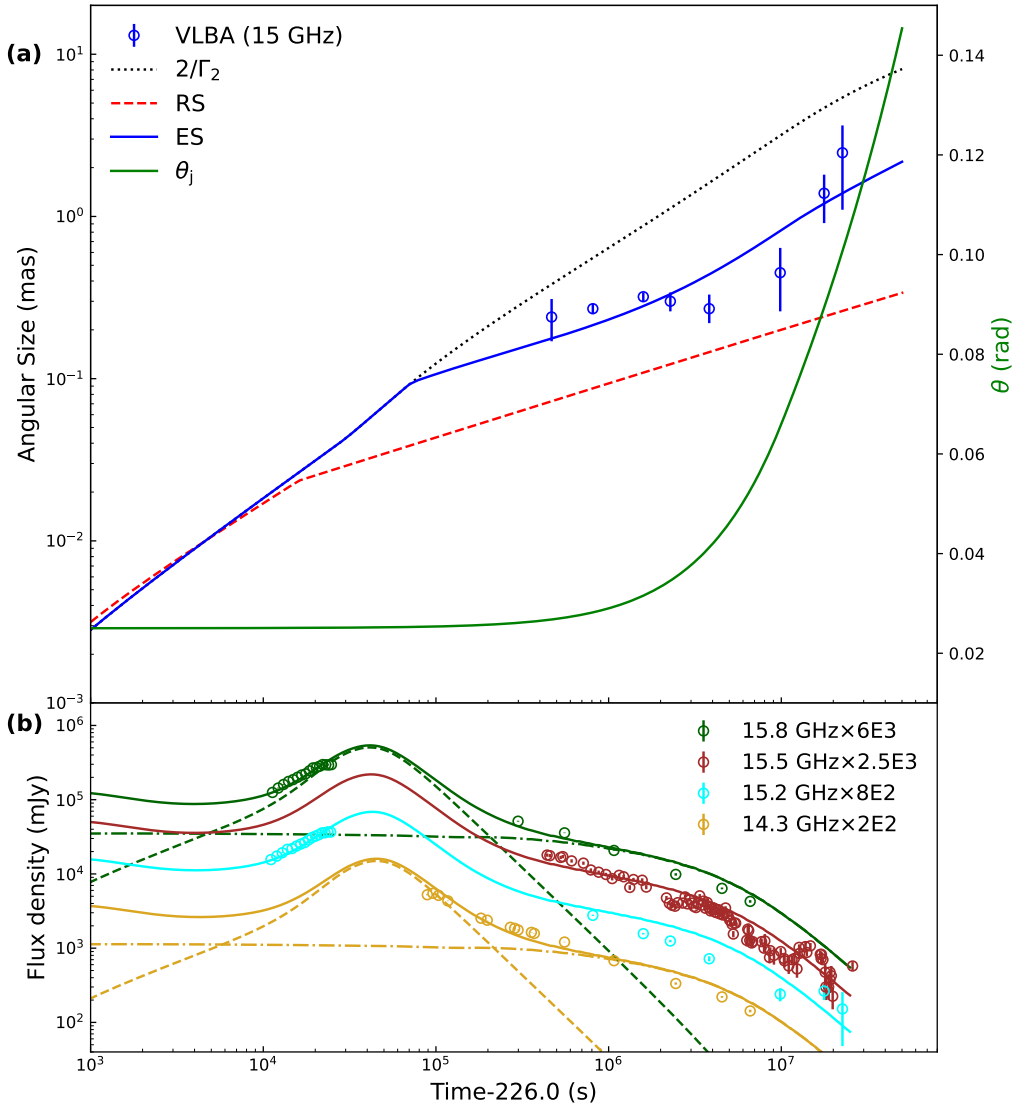


Fig. 4. Fit to the source size evolution. (a) The blue solid line and the red dashed line show the numerical size of the expanding external shock (ES) and reverse shocks (RS) lagging behind, respectively. The green line shows the evolution of the half-opening angle of the jet (ES) in the modeling (Appendix). The black dotted line represents the equivalent size area of the ES that could enter the line of sight due to the relativistic beaming effect. (b) The lightcurves around 15 GHz show that the emission of the RS (dashed lines) becomes negligible after $\sim 3 \times 10^5$ s (also see Fig. 3), hence the observed source size is determined by the emission of the ES (dash-dotted lines) afterwards.

Axelsson, M., Ajello, M., Arimoto, M., et al. 2024, arXiv e-prints, arXiv:2409.04580
 Barlow, R. 2004, arXiv e-prints, physics/0406120
 Beloborodov, A. M., & Uhm, Z. L. 2006, ApJL, 651, L1
 Blanchard, P. K., Villar, V. A., Chornock, R., et al. 2024, Nature Astronomy, arXiv:2308.14197
 Blandford, R. D., & McKee, C. F. 1976, Physics of Fluids, 19, 1130
 Blumenthal, G. R., & Gould, R. J. 1970, Rev. Mod. Phys., 42, 237

Bright, J. S., Rhodes, L., Farah, W., et al. 2023, Nature Astronomy, 7, 986
 Bromberg, O., Nakar, E., Piran, T., & Sari, R. 2011, ApJ, 740, 100
 Burns, E., Svinkin, D., Fenimore, E., et al. 2023, ApJL, 946, L31
 Castro-Tirado, A. J., Sanchez-Ramirez, R., Hu, Y. D., et al. 2022, GRB Coordinates Network, 32686, 1
 Dai, Z. G., & Gou, L. J. 2001, ApJ, 552, 72
 Dai, Z. G., & Lu, T. 1998, A&A, 333, L87

- de Ugarte Postigo, A., Izzo, L., Pugliese, G., et al. 2022, GRB Coordinates Network, 32648, 1
- Eldridge, J. J., Genet, F., Daigne, F., & Mochkovitch, R. 2006, MNRAS, 367, 186
- Fan, Y. Z., Wei, D. M., & Zhang, B. 2004, MNRAS, 354, 1031
- Foffano, L., Tavani, M., & Piano, G. 2024, ApJL, 973, L44
- Foreman-Mackey, D., Hogg, D. W., Lang, D., & Goodman, J. 2013, PASP, 125, 306
- Fraija, N., Dainotti, M. G., Betancourt Kamenetskaia, B., Galván-Gómez, A., & Aguilar-Ruiz, E. 2024, MNRAS, 527, 1884
- Frederiks, D., Svinkin, D., Lysenko, A. L., et al. 2023, ApJL, 949, L7
- Fulton, M. D., Smartt, S. J., Rhodes, L., et al. 2023, ApJL, 946, L22
- Gao, H.-X., Geng, J.-J., Sun, T.-R., et al. 2024, ApJ, 971, 81
- Geng, J.-J., Huang, Y.-F., Wu, X.-F., Zhang, B., & Zong, H.-S. 2018, ApJS, 234, 3
- Geng, J. J., Wu, X. F., Huang, Y. F., Li, L., & Dai, Z. G. 2016a, ApJ, 825, 107
- Geng, J.-J., Zhang, B., & Kuiper, R. 2016b, ApJ, 833, 116
- Ghirlanda, G., Salafia, O. S., Paragi, Z., et al. 2019, Science, 363, 968
- Giannios, D., & Spitkovsky, A. 2009, MNRAS, 400, 330
- Giarratana, S., Salafia, O. S., Giroletti, M., et al. 2024, A&A, 690, A74
- Gill, R., & Granot, J. 2023, MNRAS, 524, L78
- Gottlieb, O., Bromberg, O., Singh, C. B., & Nakar, E. 2020, MNRAS, 498, 3320
- Gottlieb, O., Nakar, E., Piran, T., & Hotokezaka, K. 2018, MNRAS, 479, 588
- Gould, R. J., & Schröder, G. P. 1967, Phys. Rev., 155, 1404
- Govreen-Segal, T., & Nakar, E. 2023, MNRAS, 524, 403
- . 2024, MNRAS, 531, 1704
- Granot, J., Guetta, D., & Gill, R. 2017, ApJL, 850, L24
- Granot, J., & Piran, T. 2012, MNRAS, 421, 570
- Granot, J., Piran, T., & Sari, R. 1999, ApJ, 513, 679
- Granot, J., Ramirez-Ruiz, E., & Loeb, A. 2005, ApJ, 618, 413
- Greisen, E. W. 2003, in *Astrophysics and Space Science Library*, Vol. 285, Information Handling in Astronomy - Historical Vistas, ed. A. Heck, 109
- Huang, Y. F., Gou, L. J., Dai, Z. G., & Lu, T. 2000, ApJ, 543, 90
- Isravel, H., Bégué, D., & Pe'er, A. 2023, ApJ, 956, 12
- Kathirgamaraju, A., Barniol Duran, R., & Giannios, D. 2018, MNRAS, 473, L121
- Kobayashi, S., & Sari, R. 2000, ApJ, 542, 819
- Kong, D.-F., Wang, X.-G., Zheng, W., et al. 2024, ApJ, 971, 56
- Kumar, P., & Granot, J. 2003, ApJ, 591, 1075
- Kumar, P., & Piran, T. 2000, ApJ, 532, 286
- Kumar, P., & Zhang, B. 2015, PhR, 561, 1
- Lamb, G. P., & Kobayashi, S. 2017, MNRAS, 472, 4953
- Laskar, T., Alexander, K. D., Margutti, R., et al. 2023, ApJL, 946, L23
- Lazzati, D., Morsony, B. J., Blackwell, C. H., & Begelman, M. C. 2012, ApJ, 750, 68
- Lazzati, D., Perna, R., Morsony, B. J., et al. 2018, PhRvL, 120, 241103
- Lesage, S., Veres, P., Briggs, M. S., et al. 2023, ApJL, 952, L42
- Levan, A. J., Lamb, G. P., Schneider, B., et al. 2023, ApJL, 946, L28
- LHAASO Collaboration, Cao, Z., Aharonian, F., et al. 2023, Science, 380, 1390
- Li, X., Yang, J., Cheng, X., et al. 2024, ApJ, 960, 1
- Lu, W., Beniamini, P., & McDowell, A. 2020, arXiv e-prints, arXiv:2005.10313
- Maciel, W. J. 2013, *General Overview of the Interstellar Medium* (New York, NY: Springer New York), 1–15. https://doi.org/10.1007/978-1-4614-3767-3_1
- Mészáros, P., Rees, M. J., & Wijers, R. A. M. J. 1998, ApJ, 499, 301
- Mooley, K. P., Anderson, J., & Lu, W. 2022, Nature, 610, 273
- Mooley, K. P., Deller, A. T., Gottlieb, O., et al. 2018, Nature, 561, 355
- O'Connor, B., Troja, E., Ryan, G., et al. 2023, Sci. Adv., 9, eadi1405
- Panaitescu, A., & Mészáros, P. 1999, ApJ, 526, 707
- Pe'er, A. 2012, ApJL, 752, L8
- Pihlström, Y. M., Taylor, G. B., Granot, J., & Doeleman, S. 2007, ApJ, 664, 411
- Planck Collaboration, Aghanim, N., Akrami, Y., et al. 2020, *Astronomy and Astrophysics*, 641, A6
- Ravasio, M. E., Salafia, O. S., Oganessian, G., et al. 2024, Science, 385, 452
- Rees, M. J., & Mészáros, P. 1998, ApJL, 496, L1
- Ren, J., Wang, Y., & Dai, Z.-G. 2024, ApJ, 962, 115
- Ren, J., Wang, Y., Zhang, L.-L., & Dai, Z.-G. 2023, ApJ, 947, 53
- Rhoads, J. E. 1999, ApJ, 525, 737
- Rhodes, L., van der Horst, A. J., Bright, J. S., et al. 2024, MNRAS, 533, 4435
- Rossi, E., Lazzati, D., & Rees, M. J. 2002, MNRAS, 332, 945

- Ryan, G., van Eerten, H., Piro, L., & Troja, E. 2020, *ApJ*, 896, 166
- Rybicki, G. B., & Lightman, A. P. 1979, *Radiative Processes in Astrophysics*, 1st edn. (New York: Wiley-Interscience Publication)
- Sari, R., & Esin, A. A. 2001, *ApJ*, 548, 787
- Sari, R., & Mészáros, P. 2000, *ApJL*, 535, L33
- Sari, R., Piran, T., & Halpern, J. P. 1999, *ApJL*, 519, L17
- Sari, R., Piran, T., & Narayan, R. 1998, *ApJL*, 497, L17
- Sato, Y., Murase, K., Ohira, Y., & Yamazaki, R. 2023, *MNRAS*, 522, L56
- Schlafly, E. F., & Finkbeiner, D. P. 2011, *ApJ*, 737, 103
- Shepherd, M. C. 1997, in *Astronomical Society of the Pacific Conference Series*, Vol. 125, *Astronomical Data Analysis Software and Systems VI*, ed. G. Hunt & H. Payne, 77
- Sironi, L., Keshet, U., & Lemoine, M. 2015, *SSRv*, 191, 519
- Sironi, L., & Spitkovsky, A. 2011, *ApJ*, 726, 75
- Taylor, G. B., Frail, D. A., Berger, E., & Kulkarni, S. R. 2004, *ApJL*, 609, L1
- Taylor, G. B., Momjian, E., Pihlström, Y., Ghosh, T., & Salter, C. 2005, *ApJ*, 622, 986
- Tchekhovskoy, A., McKinney, J. C., & Narayan, R. 2008, *MNRAS*, 388, 551
- Troja, E., Piro, L., van Eerten, H., et al. 2017, *Nature*, 551, 71
- Troja, E., van Eerten, H., Ryan, G., et al. 2019, *MNRAS*, 489, 1919
- Uhm, Z. L. 2011, *ApJ*, 733, 86
- van der Horst, A. J., Kamble, A., Resmi, L., et al. 2008, *A&A*, 480, 35
- van Eerten, H. J., & MacFadyen, A. I. 2012, *ApJ*, 751, 155
- Wang, H., Dastidar, R. G., Giannios, D., & Duffell, P. C. 2024, *ApJS*, 273, 17
- Williams, M. A., Kennea, J. A., Dichiara, S., et al. 2023, *ApJL*, 946, L24
- Wygoda, N., Waxman, E., & Frail, D. A. 2011, *ApJL*, 738, L23
- Yabe, T., Xiao, F., & Utsumi, T. 2001, *Journal of Computational Physics*, 169, 556
- Zhang, B., Fan, Y. Z., Dyks, J., et al. 2006, *ApJ*, 642, 354
- Zhang, B., & Kobayashi, S. 2005, *ApJ*, 628, 315
- Zhang, B., & Mészáros, P. 2001, *ApJL*, 552, L35
- . 2002, *ApJ*, 571, 876
- Zhang, B., Wang, X.-Y., & Zheng, J.-H. 2024, *J. High Energy Astrophys.*, 41, 42
- Zhang, B., & Yan, H. 2011, *ApJ*, 726, 90
- Zhang, B. T., Murase, K., Ioka, K., & Zhang, B. 2023, *arXiv e-prints*, arXiv:2311.13671
- Zhang, W., & MacFadyen, A. 2009, *ApJ*, 698, 1261
- Zheng, J.-H., Wang, X.-Y., Liu, R.-Y., & Zhang, B. 2024, *ApJ*, 966, 141
- Zou, Y. C., Wu, X. F., & Dai, Z. G. 2005, *MNRAS*, 363, 93

APPENDIX

VLBA OBSERVATION AND DATA REDUCTION

The pilot VLBA observation of GRB 221009A was performed at 15 GHz on October 14, 2022 (project code: TG015), ~ 5 days after the burst, with the goal of detecting the GRB and determining its precise coordinates. The accuracy of the total flux density and size measurements from TG015 was affected by a large offset between the pointing center of the observation and the actual position of the GRB. However, subsequent observations (project code: BA161) at 15 GHz at approximately 10, 19, and 26 days post-burst used a precise pointing center determined by the TG015 experiment, eliminating this influence and providing more accurate measurements of the flux density and size of this GRB.

To achieve robust detections and accurate measurements of this relatively faint source ($\sim 1\text{-}3$ mJy at 15 GHz), we implemented an optimized phase-referencing observation strategy. We used rapid switching between calibrator and target with a cycle time of 1.5 minutes (30s-60s for Cal-Tar) to overcome the phase variations at 15 GHz. This cycle time was carefully chosen based on empirical atmospheric coherence time estimates to maximize phase solution accuracy while maintaining sufficient on-source time. The data were recorded at a high rate of 4 Gbps with 512 MHz total bandwidth split into four 128 MHz intermediate frequencies, each with 256 channels. This enabled optimal data quality. The raw data were transferred to the DiFX correlator for initial processing including 2-second integration times to minimize time smearing effects.

Advanced calibration and imaging of the correlated data were executed at the China SKA Regional Centre (An et al. 2019), using a Python-based VLBI pipeline (An et al. 2022) interfacing with the Astronomical Image Processing System (AIPS) software (Greisen 2003). The process involved quality evaluation using VLBASUMM and POSSUM, with the Fort Davis antenna serving as the reference. Subsequent calibration steps corrected for Earth orientation, atmospheric factors, gain amplitudes, opacities, and detailed assessment of calibration consistency across epochs. Fringe fitting applied to the calibrator 3C 345 corrected delays and phases of the visibilities, with these corrections applied across all data. Global phase errors were determined by fringe fitting the phase calibrator J1905+1943 and corrected. Finally, bandpass functions derived from 3C 345 were applied to all data.

To ensure reliable calibration across different epochs, we maintained consistent calibration procedures and carefully evaluated potential systematic effects. We verified that the same calibrator (J1905+1943) displayed consistent fluxes between epochs (variation $< 3\%$), checked calibration solutions for systematic trends, and cross-validated results using multiple calibration approaches when possible. The systematic uncertainties from calibration were estimated to be approximately 5%, which were incorporated into our error analysis.

The calibrated J1905+1943 data were then exported to Difmap (Shepherd 1997) for self-calibration and imaging. This involved iteratively running CLEAN and phase-only self-calibration until the residual map noise level converged, followed by phase+amplitude self-calibration with shrinking solution intervals. The resulting image model enabled additional fringe fitting in AIPS to correct residual phase errors. With all calibrations applied, the target data were exported to Difmap for imaging without self-calibration due to its low signal-to-noise ratio.

We performed both circular and elliptical Gaussian fits to evaluate model-dependent uncertainties. While the source showed slight elongation in some epochs, the circular Gaussian fits provided consistent size measurements within uncertainties. The difference between circular and elliptical fits (approximately 10%) was included in our systematic error budget. This comprehensive error analysis, combining statistical and systematic uncertainties, provides robust support for the results of the evolution pattern below.

We also re-compiled the VLBI data from other work (Giarratana et al. 2024) (project code: BA160), which demonstrates the jet behavior between 44 and 262 days after the burst. VLBI observing settings of BA160 share the same parameters as BA161 on observing frequencies and bandwidth parameters. In BA160, a phase referencing cycle of 30s-30s-80s was applied for their CalA-CalB-Tar, where CalA is the major phase calibrator J1905+1943 and CalB the second phase calibrator J1925+2106. We applied the same data reduction procedure as above and used the same calibrator J1905+1943 to gain phase solutions for the target. Given that the data processing steps were not significantly different and the same major phase calibrators were employed, the systematic errors between the two observations are considered negligible. The imaging results obtained are similar to those given in previous work, demonstrating the reliability and reproducibility of our analysis (Giarratana et al. 2024).

SOURCE SIZE

We applied Markov Chain Monte Carlo (MCMC) fitting to the calibrated VLBI visibility data to extract key information including flux density, source size, and peak position (Li et al. 2024). A circular Gaussian likelihood model was adopted for simplicity. The MCMC sampling used the emcee (Foreman-Mackey et al. 2013) Python package, initialized with Difmap-derived best-fits for faster convergence. This approach was chosen to expedite the convergence of the MCMC. We ran 10^4 iterations with 8 walkers, amounting to a total of 8×10^4 evaluations of the posterior probability density. The highest-probability parameter values were taken as the best fits. One-sigma confidence ranges were defined by the 68% marginalized posterior interval. Similarly, 95% upper limits used the 95th percentile. The total flux density, relative RA, and relative DEC of the emission peak were successfully obtained from these best fits. All results are detailed in Table 1. We analyzed the BA160 epochs (B, C, C1, and D) using the same methodology as our earlier epochs. While our analysis yielded measurements consistent with those in Ref. (Giarratana et al. 2024), including a size estimate of $2.47_{-1.17}^{+1.37}$ mas for BA160D, we adopt the published values in our following analyses to maintain consistency with the peer-reviewed literature.

To model the evolution of the size data (Φ_i with 1σ uncertainties $[\sigma_{i,-}, \sigma_{i,+}]$), we employed both a power-law (PL) function and a broken power-law (BPL) function. To account for the asymmetric observational uncertainties, we utilized a weighted log-likelihood function $\ln(\mathcal{L})$, formulated as (Barlow 2004)

$$\ln(\mathcal{L}) = -\frac{1}{2}\chi^2(\vec{x}) = -\frac{1}{2}\sum_i \left[\left(\frac{\Phi(t_i; \vec{x}) - \Phi_i}{\sigma_i + \sigma'_i(\Phi(t_i; \vec{x}) - \Phi_i)} \right)^2 \right], \quad (1)$$

where $\Phi(t; \vec{x})$ represents the model size, $\sigma_i = 2\sigma_{i,+}\sigma_{i,-}/(\sigma_{i,+} + \sigma_{i,-})$ is the effective symmetric uncertainty, and $\sigma'_i = (\sigma_{i,+} - \sigma_{i,-})/(\sigma_{i,+} + \sigma_{i,-})$ accounts for the asymmetry in the errors. This formulation ensures proper handling of the non-Gaussian nature of the uncertainties.

For GRB 221009A, the PL fit yields a best-fit result of $\Phi \propto t_{\text{obs}}^{0.38}$ with a reduced chi-square (χ_{red}^2) of 4.87, while for GRB 030329, the PL fit gives $\Phi \propto t_{\text{obs}}^{0.43}$ with a χ_{red}^2 of 0.41. In contrast, the BPL fit for GRB 221009A reveals a two-stage evolution, Φ initially evolves as $t_{\text{obs}}^{0.12}$ in the slow stage, followed by a transition to a faster evolution with $t_{\text{obs}}^{2.19}$ after a transition time of $t_{\text{tr}} \simeq 10^7$ s (Fig. 2). The BPL fit achieves a χ_{red}^2 of 0.76, significantly lower than that of the single PL fit for GRB 221009A. Despite the dataset of only 8 data points – a limitation due to the inherent low-cadence sampling of VLBI observations – the notably higher χ_{red}^2 value for the single PL fit compared to the BPL fit strongly suggests that only one PL is insufficient to describe the size evolution of GRB 221009A. Instead, the data favor a two-stage evolution, as captured by the BPL.

POSSIBLE SCENARIOS FOR THE SIZE EVOLUTION

The released VLBI observations of GRB 221009A had been performed during the 40-262 days post-burst (Giarratana et al. 2024). The extrapolation of the best fitting line of these observations in 15 GHz would result in an angular diameter of $D_{\perp} \simeq 4.0 \times 10^{16}$ cm at the potential jet break time of $t_j \sim 0.8$ days (O'Connor et al. 2023), restricting the half-opening angle of the GRB jet to be

$$\theta(t_j) \simeq \frac{4ct_j}{D_{\perp}} \simeq 0.20 \left(\frac{t_j}{0.8 \text{ day}} \right) \left(\frac{D_{\perp}}{4 \times 10^{16} \text{ cm}} \right)^{-1} \text{ rad}, \quad (2)$$

which is significantly large regarding the narrow jet feature in GRB 221009A as suggested (Lesage et al. 2023; LHAASO Collaboration et al. 2023; O'Connor et al. 2023). A large lateral size at the early stage should be physically expected in return. Therefore, our observation in the early stage is crucial for understanding the jet properties of GRB 221009A. Hereafter, a flat Λ CDM model of $H_0 = 67.36 \text{ km s}^{-1} \text{ Mpc}^{-1}$ and $\Omega_m = 0.315$ is adopted (Planck Collaboration et al. 2020).

As discussed above, our early VLBA data, together with the late data (Giarratana et al. 2024), show a clear transition of the size evolution from a slow-evolving stage ($\Phi \propto t_{\text{obs}}^{0.12}$) to a fast-evolving stage ($\Phi \propto t_{\text{obs}}^{2.19}$) after a transition time of $t_{\text{tr}} \simeq 10^7$ s (Fig. 2). Below, we show that it is challenging to understand this two-stage evolution in prevalent physical scenarios (Extended Data Figure 1), implying the complex jet dynamics of GRB 221009A.

.1. The top-hat jet scenario

We start from a top-hat jet (Extended Data Figure 1a) with the isotropic kinetic energy of $E_{K,\text{iso}}$, the initial bulk Lorentz factor of Γ_0 and half-opening angle of $\theta_{j,0}$ propagating in a circumburst medium with a power-law profile

$\propto R^{-s}$, where R is the distance from the explosion center. The jet begins to decelerate significantly when the blastwave sweeps a certain amount of materials, and the deceleration timescale is

$$t_{\text{dec}} \simeq \begin{cases} 10^2 \left(\frac{E_{\text{K,iso}}}{10^{55} \text{ erg}} \right)^{1/3} \left(\frac{\Gamma_0}{300} \right)^{-8/3} \left(\frac{n_{\text{ISM}}}{0.1 \text{ cm}^{-3}} \right)^{-1/3} \text{ s} & \text{for ISM,} \\ 40 \left(\frac{E_{\text{K,iso}}}{10^{55} \text{ erg}} \right) \left(\frac{\Gamma_0}{300} \right)^{-4} \left(\frac{A_*}{0.1} \right)^{-1} \text{ s} & \text{for Wind,} \end{cases} \quad (3)$$

where n_{ISM} is the ISM number density and A_* is the dimensionless wind parameter. Our observation epochs ($t_{\text{obs}} > 10^5$ s) should be at the deceleration stage of the jet with $\Gamma_0 \geq 30$ applicable to both the interstellar medium (ISM, $s = 0$) and the wind-like environment ($s = 2$). During this stage, the jet dynamics well obeys the Blandford-McKee (BM) solution (Blandford & McKee 1976), i.e., $R \propto t_{\text{obs}}^{1/(4-s)}$ and $\Gamma \propto t_{\text{obs}}^{(s-3)/(8-2s)}$, where Γ is the bulk Lorentz factor. Assuming that $\theta_j = \theta_{j,0}$ is maintained during its propagation, one could expect the projected size to be $\Phi = 2R \sin(\min[\Gamma^{-1}, \theta_{j,0}])/D_A$, i.e.,

$$\Phi \propto \begin{cases} t_{\text{obs}}^{5/8} & \text{for } t_{\text{obs}} < t_j, \\ t_{\text{obs}}^{1/4} & \text{for } t_{\text{obs}} \geq t_j, \end{cases} \quad (4)$$

for $s = 0$, or

$$\Phi \propto \begin{cases} t_{\text{obs}}^{3/4} & \text{for } t_{\text{obs}} < t_j, \\ t_{\text{obs}}^{1/2} & \text{for } t_{\text{obs}} \geq t_j, \end{cases} \quad (5)$$

for $s = 2$, where Γ^{-1} represents the region that is visible due to the beaming effect, t_j is the well-known jet break time for $\Gamma(t_j) = \theta_{j,0}^{-1}$, and D_A is the cosmological angular diameter distance. The possible jet break constrained by the TeV (LHAASO Collaboration et al. 2023) or the X-ray/Optical (O'Connor et al. 2023) lightcurves indicates that t_j is less than $\sim 10^5$ s. The resulting evolution law of $\Phi \propto t_{\text{obs}}^{1/4}$ in the ISM is more consistent with the slow-evolving stage than that of $\Phi \propto t_{\text{obs}}^{1/2}$ in the wind-like medium (Extended Data Figure 2). However, the relatively shallow decaying index of the X-ray and optical afterglow prefers the wind environment (Ren et al. 2023; O'Connor et al. 2023). Moreover, theoretical rates of size evolution in both cases are much slower than the observed fast-evolving stage. Therefore a simple non-spreading top-hat jet is insufficient to explain the observations.

Nonetheless, it is clear that all size values are greater than 0.2 mas after 10^6 s at a 3σ confidence level (Fig. 2), putting a robust constraint on the jet angle of

$$\theta_{j,0} \geq 0.15 \left(\frac{E_{\text{K,iso}}}{10^{55} \text{ erg}} \right)^{-1/4} \left(\frac{n_{\text{ISM}}}{1 \text{ cm}^{-3}} \right)^{1/4} \left(\frac{\Phi}{0.2 \text{ mas}} \right) \left(\frac{t_{\text{obs}}}{10^6 \text{ s}} \right)^{-1/4} \text{ rad}, \quad (6)$$

and

$$\theta_{j,0} \geq 0.01 \left(\frac{E_{\text{K,iso}}}{10^{55} \text{ erg}} \right)^{-1/2} \left(\frac{A_*}{0.1} \right)^{1/2} \left(\frac{\Phi}{0.2 \text{ mas}} \right) \left(\frac{t_{\text{obs}}}{10^6 \text{ s}} \right)^{-1/2} \text{ rad}, \quad (7)$$

respectively. Considering the narrow jet nature ($\theta_{j,0} < 0.1$) supported by other evidences (Burns et al. 2023; Williams et al. 2023; O'Connor et al. 2023), these lower limits strengthen that the jet should undergo an early fast-moving episode in the wind environment to reach the observed size level, which is significantly larger than that of GRB 030329 (Fig. 2). As $E_{\text{K,iso}}$ should not significantly exceed the prompt emission energy of 10^{55} erg in such bright burst, and a range of $A_* \geq 0.1$ were commonly adopted in the afterglow modeling (Gill & Granot 2023; Ren et al. 2024; Zheng et al. 2024), Eq. (7) provides a robust lower limit of $\theta_{j,0} \geq 0.01$ for GRB 221009A.

2. The structured jet scenario

Rather than a top-hat jet, the realistic jet may be structured (Extended Data Figure 1b), formed either by the launching process of the central engine or interactions between the jet and the star envelope (Tchekhovskoy et al. 2008; Lazzati et al. 2012; Geng et al. 2016b; Gottlieb et al. 2020). As commonly adopted in the literature, the distribution of the equivalent isotropic kinetic energy and the initial bulk Lorentz factor is assumed to be a constant within the jet core (θ_c), while it follows a power-law distribution beyond the jet core, i.e., $E_{\text{K,iso}}(\theta) \propto \theta^{-k_E}$ and $\Gamma_0(\theta) \propto \theta^{-k_\Gamma}$ for $\theta_c < \theta \leq \theta_{\text{edge}}$. For the period we focus on, the evolution of the bulk Lorentz factor at different latitudes enters the BM self-similarity regime at $t_{\text{obs}} > 10^5$ s (Equation (3)), hence the profile of $\Gamma_0(\theta)$ would not affect

the analyses below. If the jet continues to be mildly relativistic at large latitudes, the observed source size is defined by the size when different latitudes enter the field of view due to gradual deceleration. Using $\Gamma(\theta, t_{\text{obs}}) = \theta^{-1}$ and considering the BM solution for Γ , the observed size evolution may be written as

$$\Phi \propto \begin{cases} t_{\text{obs}}^{(5-k_E)/(8-k_E)}, & \text{for } s = 0, \\ t_{\text{obs}}^{(3-k_E)/(4-k_E)}, & \text{for } s = 2. \end{cases} \quad (8)$$

The temporal indices could range from negative infinity to positive infinity mathematically. However, k_E lies within three intervals separated by two critical values for different physical situations. Taking $s = 0$ as an example, for an interval of $k_E \in [8, \infty)$, it corresponds to an image of a luminous core and an outer dim ring with its inner radius expanding inward. The outer dim ring is undetectable ($E_{K,\text{iso}} \propto \theta^{-k_E}$) and it does not affect the size evolution. In the interval of $k_E \in [4, 8]$, its wing size grows shallower than that of the jet core, so the observed whole size is dominated by the fast-growing core, asymptotic as a top-hat jet (Extended Data Figure 2). The third interval of interest, $k_E \in [0, 4]$, corresponds to situations ranging from the extended spherical regime (of a top-hat jet with angle of θ_{edge}) to the jet-like regime (of a top-hat jet with angle of θ_c). If we attribute the two-stage size evolution to the structured jet in the ISM, it mathematically requires a BPL structure with two indices of $k_E = 4.59_{-0.29}^{+0.25}$ and $k_E = 10.52_{-1.15}^{+4.30}$ for two stages, respectively. However, these required k_E are greater than the critical value of 4, above which the temporal indices should tend to and could not be shallower than that of a top-hat jet, as it implies that the size is dominated by the inner uniform core. Similarly, $k_E = 2.86_{-0.10}^{+0.08}$ and $k_E = 4.84_{-0.38}^{+1.43}$ are required at the two stages and the dilemma also holds for the wind case. Moreover, k_E derived mathematically in the early slow stage is much larger than that indicated from the afterglow modeling (O'Connor et al. 2023; Zheng et al. 2024).

Suppose that the wing edge of the inner segment comes into the line of sight near $t_{\text{tr}} \simeq 10^7$ s. The duration of the slow stage further gives

$$\frac{\theta_{\text{edge}}}{\theta_c} \propto \begin{cases} \left(\frac{t_{\text{tr}}}{t_{j,c}}\right)^{3/(8-k_E)}, & \text{for } s = 0, \\ \left(\frac{t_{\text{tr}}}{t_{j,c}}\right)^{1/(4-k_E)}, & \text{for } s = 2, \end{cases} \quad (9)$$

where $t_{j,c}$ is the jet break time of the core. Since $t_{j,c}$ is less than $\sim 10^5$ s in the wind modeling (O'Connor et al. 2023), $\theta_{\text{edge}}/\theta_c$ is roughly 50 with $k_E = 2.86$ and the equivalent isotropic kinetic energy near the edge drops by a factor of $\gtrsim 10^4$. This means the wing should be too dim to affect the whole size evolution, consistent with the discussion above. Note that Equation (8) is valid only when $\Gamma(\theta)$ is in the mildly relativistic range for large θ at a late stage. Hence the profile of Γ_0 need be shallow, i.e., $k_\Gamma \lesssim 1$. Otherwise, the emitting sites at large θ are within our sight very soon and the source size is actually determined by the inner faster and leading core of the jet lately, with an asymptotic behavior similar to that of a top-hat jet. Therefore, a structured jet with the initial conventional profile is difficult to interpret the observed two-stage size evolution.

.3. The spreading jet scenario

It is possible that the relativistic jet of GRB 221009A may be evolving itself (Extended Data Figure 1c). The relativistic jet propagates as the BM solution and keeps well collimated due to the lack of transverse causal connection within t_j . As the jet has to transition to non-relativistic at t_{NR} and spread to nearly spherical in the Sedov-Taylor phase, precise modeling of the spreading process is important but remains uncertain in the literature (Zhang & MacFadyen 2009; Wygoda et al. 2011; van Eerten & MacFadyen 2012; Granot & Piran 2012; Lazzati et al. 2018; Lu et al. 2020; Govreen-Segal & Nakar 2023, 2024; Wang et al. 2024). We assume that significant lateral spreading may occur when the jet Lorentz factor approaches $\zeta/\theta_{j,0}$ (Rhoads 1999; Sari et al. 1999; Granot & Piran 2012), where ζ is a dimensionless parameter less than unity and its accurate value is still uncertain in the literature. The degree of the lateral-spreading strongly depends on $\theta_{j,0}$, varying between the slow spreading case (Panaitescu & Mészáros 1999; Rhoads 1999; Granot et al. 2005) and the fast spreading case (Zhang & MacFadyen 2009; Wygoda et al. 2011; Granot & Piran 2012; Govreen-Segal & Nakar 2023, 2024) (Extended Data Figure 2). If we attribute the observed slow-evolving stage to a top-hat jet, the fast spreading could in principle account for the fast-evolving stage of the size. Then the Γ evolution in the slow stage indicates that

$$\zeta \simeq \left(\frac{t_{\text{sp}}}{t_j}\right)^{(s-3)/(8-2s)}, \quad (10)$$

placing the upper limit of ζ as $\zeta \leq 0.3$ and $\zeta \leq 0.5$ for the ISM and the wind cases, respectively. Note that our VLBI observations indicate that $t_{\text{sp}} \simeq 10^7$ s and $t_j \leq 5 \times 10^5$ s.

In the fast spreading scenario, the radius when the blastwave gets non-relativistic could be estimated as (Granot & Piran 2012) $R_{\text{NR}} \simeq (1 - \ln \theta_{j,0}) R_{\text{sp}}$, which further gives

$$t_{\text{NR}} = \left[(1 - \ln \theta_{j,0}) \frac{\sin \theta_{\text{NR}}}{\sin \theta_{j,0}} \right]^{1/q} t_{\text{sp}}, \quad (11)$$

where q is the observed temporal expansion rate (1σ region of [1.44, 3.19]) and θ_{NR} is the half-opening angle of the jet approaching the non-relativistic phase (van der Horst et al. 2008). Assuming $\theta_{\text{NR}} \sim 0.5$ and $\theta_{j,0} \simeq 0.01$ for GRB 221009A, we get $t_{\text{NR}} \in [2, 15]$ years for the expansion rate derived from our fit.

Although analytical analyses and hydrodynamic simulations show that the jet opening angle could increase rapidly in the lateral spreading regime, it is still uncertain whether the resulting projected size of the jet could evolve as steeply as observed in GRB 221009A, since its bulk Lorentz factor would also reduce rapidly at the same time. More detailed hydrodynamic simulations on this issue are encouraged.

4. Emergence of a new emission component from large latitudes

Another possibility is that the slow-evolving stage is attributed to a top-hat jet or a structured jet with large k_E , while the fast-evolving stage is caused by the emergence of another emission component appearing abruptly at larger latitudes at the late stage (Extended Data Figure 1d). The absence of a significant shift of the centroid of the radio image indicates this component should be concentric with the inner component, e.g., another concentric wider jet with an inner edge angle of θ_2 . At the jet break time of the wide component, $t_{j,2}$, the bulk Lorentz factor of the wide jet is

$$\Gamma_{j,2} \simeq \frac{D_{\perp}}{4ct_{j,2}} = 4.2 \left(\frac{D_{\perp}}{10^{19} \text{ cm}} \right) \left(\frac{t_{j,2}}{2 \times 10^7 \text{ s}} \right)^{-1}, \quad (12)$$

as inferred from Fig. 2. The corresponding edge angle is $\theta_2 \simeq \Gamma_{j,2}^{-1} \simeq 0.24$ rad. On the other hand, the equivalent isotropic energy of the wide jet should satisfy a ratio of

$$\frac{E_{\text{K,iso},2}}{E_{\text{K,iso},1}} \simeq \left(\frac{\theta_{j,0}}{\theta_2} \right)^{2(4-s)} \left(\frac{t_{j,1}}{t_{j,2}} \right)^{s-3}. \quad (13)$$

For $t_{j,2}/t_{j,1} \geq 10^2$ constrained from observations, the jet energy ratio is $E_{\text{K,iso},2}\theta_2^2/E_{\text{K,iso},1}\theta_{j,0}^2 \gtrsim 1$ if a conservative value of $\theta_2/\theta_{j,0} \simeq 10$ is adopted, both for $s = 0$ or $s = 2$. The required large jet energy from the outer wide jet has not been predicted from previous numerical simulations (Lazzati et al. 2012). Such a component, if exists, may require additional physical mechanism to launch. The size evolution of the wide component after $t_{j,2}$ is again similar to that of a top-hat jet, the long-term monitoring could verify this scenario.

5. Emergence of a new emission component due to central engine energy injection

Yet another possibility is that the fast-evolving stage is powered by a new emerging component with late-time energy injection from the central engine, after the emission of the early jet declines significantly. This component should still be mildly relativistic at late time to have a comparable radius as that of the early jet. The injection could be in the form of long-term engine injection (Dai & Lu 1998; Zhang & Mészáros 2001) or spreading in bulk Lorentz factor (Rees & Mészáros 1998; Sari & Mészáros 2000). The two descriptions may be observationally equivalent (Zhang et al. 2006). We consider the case of continuous energy injection from the engine. Its bulk Lorentz factor can be written as $\Gamma \propto t_{\text{obs}}^{-(2-\delta)/8}$ for the ISM and $\Gamma \propto t_{\text{obs}}^{\delta/4}$ for the wind, where the injected luminosity is taken as $L_{\text{inj}} \propto t_{\text{obs}}^{\delta}$ (Zhang & Mészáros 2001). For $\delta \geq 2$ in the ISM or $\delta \geq 0$ in the wind, Γ could keep constant, hence the corresponding observed size could be steeper than $\Phi \propto t_{\text{obs}}^1$. However, $\delta < 0$ is usually expected for various well-discussed energy injection processes, such as fall-back accretion, dipolar spin-down etc. This scenario therefore also requires unconventional parameters to account for the data.

MODELING OF MULTI-WAVELENGTH EMISSIONS

Based on the analyses of the size observation above, we move to interpret the complex temporal and spectral behaviors of GRB 221009A and see how our observations promote our understanding of the origin of the multi-wavelength emissions.

6. External shock scenario

In the standard external shock scenario (Sari et al. 1998), the interstellar medium is shocked by a blastwave with a bulk Lorentz factor of Γ , and accelerated electrons emit multi-wavelength photons through synchrotron radiation. Assuming the distribution of the accelerated electrons is a power-law with an index of p and a minimum Lorentz factor of γ_m , the synchrotron radiation of these electrons will shine in the X-ray, optical, and radio bands over time, as electrons cool in the comoving frame magnetic field of B' (the superscript of $'$ denotes the quantities in the comoving frame hereafter). The cooling Lorentz factor $\gamma_c = \frac{6\pi m_e c(1+z)}{\sigma_T \Gamma B'^2 (1+Y) t_{\text{obs}}}$ is thus commonly introduced to describe the evolving electron spectrum, where m_e is the electron mass, c is the speed of light, σ_T is the Thomson cross-section, and Y is the Compton parameter defined as the ratio of the inverse Compton power to the synchrotron power. These two characteristic frequencies, $\nu_m \propto \Gamma B' \gamma_m^2$ and $\nu_c \propto \Gamma B' \gamma_c^2$, together with the peak flux density $F_{\nu, \text{max}}^{\text{Syn}} \propto \Gamma N_e B'$ by a total of N_e electrons, could well define the observed synchrotron spectra shape (Sari et al. 1998, 1999). In addition, synchrotron photons would Compton scatter on electrons, producing an inverse Compton (IC) component at higher energies. IC scattering by self-emitted synchrotron photons is referred as the synchrotron self-Compton (SSC) process, and the corresponding spectra could also be approximated as a broken power law with characteristic frequencies of $\nu_m^{\text{IC}} = 2\gamma_m^2 \nu_m$ and $\nu_c^{\text{IC}} = 2\gamma_c^2 \nu_c$, and a peak flux of $F_{\nu, \text{max}}^{\text{IC}} \simeq x_0 \sigma_T n_{\text{ISM}} R F_{\nu, \text{max}}^{\text{Syn}}$, where $x_0 \sim 0.5$ is a correction factor, n_{ISM} is the number density of interstellar medium (Sari & Esin 2001).

Below, we show that the early temporal behavior in the TeV and the optical band of GRB 221009A could not be simultaneously interpreted within the simple external shock scenario. For the slow cooling case ($\nu_m < \nu_c$), the flux density at TeV range writes as $F_\nu^{\text{IC}} = F_{\nu, \text{max}}^{\text{IC}} \frac{p-1}{p+1} \left(\frac{\nu_c}{\nu_m}\right) \left(\frac{\nu}{\nu_m^{\text{IC}}}\right)^{-p/2}$. The peak time of the TeV lightcurve, $t_{\text{TeV, Peak}}$, corresponds to the end time of the early coasting phase of blastwave ($\Gamma \simeq \Gamma_0 = \text{const}$), when the blastwave sweeps comparable materials (Sari et al. 1998), i.e.,

$$E_{\text{K, iso}} = \frac{32\pi}{3} m_p c^5 n_{\text{ISM}} \Gamma_0^8 t_{\text{TeV, Peak}}^3, \quad (14)$$

where $E_{\text{K, iso}}$ is the initial isotropic kinetic energy of the blastwave. During this phase, we have $F_\nu^{\text{IC}} \propto x_0(1+Y)^{-2} \epsilon_e^{2p-2} \epsilon_B^{(p-6)/4} E_{\text{K, iso}}^{(3p+2)/8} n_{\text{ISM}}^{(2-p)/8} t_{\text{TeV, Peak}}^{-3(3p+2)/8} \nu^{-p/2} t_{\text{obs}}^2$, where ϵ_e and ϵ_B are equipartition parameters for shocked electrons and magnetic field respectively. After the coasting phase, Γ evolves as $\propto t_{\text{obs}}^{-3/8}$ by the BM solution (Blandford & McKee 1976). At the decreasing phase, the synchrotron radiation at the optical band could write as $F_\nu^{\text{Syn}} \propto \epsilon_B^{(p+1)/4} \epsilon_e^{p-1} n_{\text{ISM}}^{1/2} E_{\text{K, iso}}^{(p+3)/4} \nu^{-(p-1)/2} t_{\text{obs}}^{-3(p-1)/4}$ for $\nu_m < \nu < \nu_c$. Therefore, the ratio between the optical flux at t_{obs} and the TeV peak flux is

$$\begin{aligned} \frac{F_{\text{Opt}}^{\text{Syn}}(t_{\text{obs}})}{F_{\text{TeV, Peak}}^{\text{Syn}}} &\simeq 4 \times 10^8 x_0^{-1} (1+Y)^2 \left(\frac{\epsilon_B}{6 \times 10^{-4}}\right)^{7/4} \left(\frac{\epsilon_e}{0.025}\right)^{1-p} \left(\frac{n_{\text{ISM}}}{0.4 \text{ cm}^{-3}}\right)^{(2+p)/8} \\ &\times \left(\frac{E_{\text{K, iso}}}{1.5 \times 10^{55} \text{ erg}}\right)^{(4-p)/8} \left(\frac{\nu_{\text{Opt}}}{4.7 \times 10^{14} \text{ Hz}}\right)^{-(p-1)/2} \left(\frac{\nu_{\text{TeV}}}{1.62 \text{ TeV}}\right)^{p/2} \\ &\times \left(\frac{t_{\text{TeV, Peak}}}{20 \text{ s}}\right)^{(9p-10)/8} \left(\frac{t_{\text{obs}}}{4000 \text{ s}}\right)^{-3(p-1)/4} \end{aligned} \quad (15)$$

for $p = 2.2$ constrained from the spectrum and other microphysical parameters same as those adopted by LHAASO Collaboration (LHAASO Collaboration et al. 2023). However, the earliest observed flux in r band at ~ 4000 s after burst gives a ratio of 4×10^7 . Except for the theoretical flux excess in the optical band, a similar flux excess in the radio flux arises only if we attribute the whole TeV emission to the standard external shock in ISM.

The accurate jet dynamic and possible jet break effect are not considered in the estimations above. Also, it is difficult to account for the nonlinear effects like IC scattering in the Klein–Nishina regime (Blumenthal & Gould 1970) and photon-photon annihilation (Gould & Schröder 1967) accurately under analytical approximation. Hence we performed detailed numerical calculations to demonstrate the conflict in the explanation of early multi-wavelength data using the external shock scenario. A generic model based on energy conservation is adopted to describe the dynamic of the external shock (Huang et al. 2000; Pe'er 2012). The time-dependent electron spectrum shocked by the blastwave is calculated by solving the continuity equation in the energy space, i.e.,

$$\frac{\partial}{\partial t'} \left(\frac{dN_e}{d\gamma'_e} \right) + \frac{\partial}{\partial \gamma'_e} \left[\dot{\gamma}'_{e, \text{tot}} \left(\frac{dN_e}{d\gamma'_e} \right) \right] = Q(\gamma'_e, t'), \quad (16)$$

using the constrained interpolation profile method (Yabe et al. 2001; Geng et al. 2018), where $\dot{\gamma}'_{e,\text{tot}} = \dot{\gamma}'_{e,\text{syn}} + \dot{\gamma}'_{e,\text{adi}}$ is the energy loss rate consisting of synchrotron radiation and adiabatic cooling, $Q(\gamma'_e, t') \propto (\gamma/\gamma_m)^{-p}$ is the source function that describes the electrons shocked into the emitting shell. Synchrotron power $P'_{\text{Syn}}(\nu')$ and the SSC power $P'_{\text{SSC}}(\nu'_{\text{ic}})$ from these electrons could be obtained by integrating the electron spectrum using the standard formulae (Rybicki & Lightman 1979). In addition, the synchrotron self-absorption for radiation at low frequencies and the photon-photon annihilation at a high-energy range are included. At last, the observed multi-wavelength emission is obtained by integrating the equal-arrival-time surface (Granot et al. 1999), and a set of five free parameters ($E_{\text{K,iso}}$, Γ_0 , ϵ_e , ϵ_B , n_{ISM}) could be derived from the standard Bayesian framework.

Since the flux in low frequencies is sensitive to the jet opening angle, three different sets of calculations are performed. First, we take an initial opening angle $\theta_{j,0}$ of 0.01 rad and apply the standard model to fit the TeV lightcurve and spectra in five time intervals and the early X-ray lightcurve ($< 10^3$ s). The best fitting results (Supplementary Table 1) show the flux excess in the early optical and radio band (Extended Data Figure 3a) at the 3σ level. A narrower jet ($\theta_{j,0} = 0.005$) is further considered and only the TeV lightcurve and spectra are used in the fitting. Although the optical and radio flux decline rapidly after the jet break, the excess in the early optical and radio band still holds (see Extended Data Figure 3b). Even $E_{\text{K,iso}}$ is fixed to a relatively smaller value (9×10^{54} erg), this issue could not be eliminated in the third calculation (Extended Data Figure 3c). Other attempts, like exploring the effect that only a portion (e.g., 10%) of electrons are accelerated to emit, also failed. The lower limit of $\theta_{j,0}$ as given in Equation (6) by VLBI information makes this issue more severe. Therefore, we confirm that if the TeV emission purely comes from the external shock propagating in the ISM, particles that produce TeV photons would give brighter optical and radio emissions when they cool down. The possible jet configuration of an inner jet core and a surrounding wing component also suffers from such an issue since the slower wing tends to contribute more emissions at low frequencies.

7. The two-shell collision scenario

To overcome the flux excess issue and give a self-consistent explanation for the multi-wavelength emission of GRB 221009A, we propose the two-shell collision scenario (Kumar & Piran 2000), in which the early main TeV emission comes from the shock interactions during the prompt phase. Given that the strong pulse of prompt emission released at $\sim T_0 + 185$ s would launch a preceding outflow before the onset of TeV emission ($\sim T_0 + 225$ s), the inevitable collision between this initial flow and a subsequent, more energetic outflow should play a crucial role. As the preceding outflow decelerated to a bulk Lorentz factor of Γ_1 , a later launched but faster shell (with a bulk Lorentz factor of Γ_4) will catch up at radius R_0 , colliding with the slow shell. If the fast shell is not extremely magnetized, the collision would produce a forward shock (FS) propagating into materials of the preceding shell, and a reverse shock (RS) propagating into the fast shell. After crossing the slow shell, the FS will break out into the circumburst material, becoming an external shock (ES), which produces long-lasting afterglows (see an illustration for this scenario in Extended Data Figure 4). Through detailed numerical modeling, we show that this two-shell collision scenario could self-consistently explain the rich observations of GRB 221009A.

Modeling of the shock dynamics During the collision, two shocks separate the system into four regions: (1) the unshocked slow shell, (2) the shocked slow shell, (3) the shocked fast shell, and (4) the unshocked fast shell. Hereafter, χ_i denotes the value of the quantity χ in Region “ i ” in its own rest frame (also see Extended Data Figure 4), and χ_{ij} denotes the value of the quantity χ in Region “ i ” measured in the rest frame of Region “ j ”. Unlike the preceding shell that exhausts the magnetic energy in the early stage ($\sigma_1 \simeq 0$), the later fast shell may keep the magnetic fields advected from the central engine, which could be parameterized by the magnetization of

$$\sigma_4 = \frac{B_4^2}{4\pi n_4 m_p c^2}, \quad (17)$$

where n_4 is the particle density in the comoving frame of Region 4. Let’s introduce an equivalent “luminosity” of the total energy for the two shells measured in the lab frame, L_1 and L_4 , the particle density is then

$$n_i = \frac{L_i}{4\pi R^2 \beta_i \Gamma_i^2 m_p c^3 \left[1 + \frac{4}{3}(\gamma_{p,i} - 1)\right] (1 + \sigma_i)}, \quad (18)$$

where $i = 1, 4$, $\beta_i = 1/\sqrt{1 - 1/\Gamma_i^2}$, and $\gamma_{p,i}$ is the average Lorentz factor of protons in each upstream. The particles in Region 1 are supposed to be shocked or heated already, i.e., $\gamma_{p,1} > 1$, while the later outflow is cold ($\gamma_{p,4} = 1$). The adiabatic cooling of hot protons is described by $\gamma_{p,1} \propto (R/R_0)^{-2/3}$. For simplicity, both the luminosity of the two shells

are assumed to be constant, i.e., $L_4 = L_f$ before RS crossing ($R < R_{\text{off},3}$) and $L_1 = L_s$ before FS crossing ($R < R_{\text{off},2}$). We also assume that Region 2 and Region 3 share a common bulk Lorentz factor ($\Gamma_2 = \Gamma_3$). After applying the hydrodynamical/magnetohydrodynamical jump conditions (Kumar & Piran 2000; Fan et al. 2004; Zhang & Kobayashi 2005) to the FS/RS respectively and the energy conservation law to the FS-RS system (Beloborodov & Uhm 2006; Uhm 2011; Geng et al. 2016a; Ai & Zhang 2021), the evolution of Γ_2 and relevant quantities within these regions could be solved numerically. For an infinitesimal radius increment of dR , the RS will sweep $dN_3 = 4\pi R^2 n_4 \Gamma_4 dR (\beta_4 - \beta_{\text{RS}}) / \beta_2$ particles into Region 3, while the FS would sweep $dN_2 = 4\pi R^2 n_1 \Gamma_1 dR (\beta_{\text{FS}} - \beta_1) / \beta_2$ particles into Region 2, where β_{FS} and β_{RS} are the velocities of the FS and RS. Given the initial total isotropic energy of each shell ($E_{\text{iso},f}$ and $E_{\text{iso},s}$), the energy conservation of $E_f = \Gamma_4 m_p c^2 (1 + \sigma_4) \int_{R_0}^{R_{\text{off},3}} dN_3$ and $E_s = \Gamma_1 [4/3(\gamma_{p,1} - 1) + 1] m_p c^2 \int_{R_0}^{R_{\text{off},2}} dN_2$ determines the radius that the RS and the FS cross each shell, i.e., $R_{\text{off},3}$ and $R_{\text{off},2}$ respectively.

After the RS crossing, the shocked Region 3 will detach from Region 2 when the effective thermal Lorentz factor of the plasma is approaching 1 due to the adiabatic expansion. After the detachment, the bulk Lorentz factor of Region 3 could be modeled as $\Gamma_3 \propto R^{-g}$, where $g \in [1/2, 3/2]$ and its exact value should be determined from hydrodynamic simulations (Kobayashi & Sari 2000; Zou et al. 2005). However, as function of the observed time, $\Gamma_3(t_{\text{obs}})$ is not very sensitive to the exact value of g , hence a median value of $g = 1$ is taken in our calculations.

According to the particle-in-cell simulations for shocks (Sironi & Spitkovsky 2011; Sironi et al. 2015), the distribution of the accelerated electrons downstream could be generalized as

$$Q(\gamma'_e, t') = \begin{cases} Q_{\text{inj}}(t') \left(\frac{\gamma'_e}{\gamma'_{\text{th}}}\right)^2 \exp\left(-\frac{\gamma'_e}{\gamma'_{\text{th}}}\right), & \gamma'_e \leq \gamma'_{\text{nth}}, \\ Q_{\text{inj}}(t') \left(\frac{\gamma'_{\text{nth}}}{\gamma'_{\text{th}}}\right)^2 \exp\left(-\frac{\gamma'_{\text{nth}}}{\gamma'_{\text{th}}}\right) \left(\frac{\gamma'_e}{\gamma'_{\text{nth}}}\right)^{-p}, & \gamma'_e > \gamma'_{\text{nth}}, \end{cases} \quad (19)$$

where Q_{inj} is the normalized injection rate, γ'_{th} and γ'_{nth} are the characteristic thermal and non-thermal Lorentz factors in the comoving frame respectively (Giannios & Spitkovsky 2009; Gao et al. 2024). By introducing the energy fraction parameter of the non-thermal part to the total energy δ , γ'_{th} and γ'_{nth} could be solved from known ϵ_e and shock jump conditions. In our scenario, such a generalized electron distribution is adopted for all shocked regions, and the emissions from these regions are subsequently obtained.

Size modeling As mentioned above, the VLBI observation prefers that the jet is propagating in the ISM beyond 5×10^5 s post burst. On the contrary, the shallow decay of early ($< 10^5$ s) optical emissions supports that the jet was propagating in the wind medium with varying number densities of

$$n(t_{\text{obs}}) = 8 \times 10^{-4} \left(\frac{E_{\text{K,iso}}}{10^{55} \text{ erg}}\right)^{-1} \left(\frac{A_*}{0.5}\right)^2 \left(\frac{t_{\text{obs}}}{10^5 \text{ s}}\right)^{-1} \text{ cm}^{-3}, \quad (20)$$

which becomes sufficiently smaller than the typical value of the ISM $\sim 0.1 \text{ cm}^{-3}$ (Maciel 2013). Meanwhile, the burst is sited at a dense star formation region as revealed by the James Webb Space Telescope (JWST) observation (Blanchard et al. 2024). Therefore, these evidences point out that the circumburst environment of GRB 221009A should transit from the wind type to the ISM, a common expectation in GRBs (Eldridge et al. 2006). In our modeling, the jet encounters the ISM beyond the terminal radius (R_T), and a smooth transition is adopted for simplicity, i.e., $n_{\text{ISM}} = 3 \times 10^{35} A_* \text{ cm}^{-1} / R_T^2$ for $R > R_T$.

The fast size evolution indicates the significant lateral expansion of the jet at late times, which holds for jets with extremely narrow jet angles. For the top-hat jet approximation considered here, the increasing rate of the half-opening angle could be described as (Granot & Piran 2012)

$$\frac{d\theta_j}{d \ln R} = \frac{1}{\Gamma^2 \theta_j}, \quad (21)$$

which is incorporated in the equations mentioned in S4.3 to determine the dynamics of a spreading jet consistently. Although the jet angle spreads exponentially, the bulk Lorentz factor decreases faster than the BM solution as it sweeps more materials, resulting in a power-law like numerical expansion exhibited in Fig. 4.

The source size evolution has been argued to be frequency-dependent, due to the transition from being dominated by the RS emission to being dominated by the ES emission (Giarratana et al. 2024). However, it is shown that the light curve at 15 GHz is already dominated by the radiation of the ES beyond $\sim 3 \times 10^5$ s (see Fig. 3). Meanwhile,

the RS lags far behind the ES, and its projected size, if visible, should be much smaller than observed values, as also shown in Fig. 4. Thus it is reasonable to model the observed size at 15 GHz using the ES directly.

Temporal and spectral modeling The temporal evolution consists of three stages. In the first stage of collision, the FS produces the main peak of the TeV emission through the SSC process. For $\Gamma_f \gg \Gamma_s \gg 1$, the collision starts at $R_0 \approx 2\Gamma_s^2 c \Delta t \simeq 10^{15}$ cm with $\Gamma_s \simeq 50$ and $\Delta t \simeq \mathcal{O}(10)$ s. In the second stage, the FS turns into the ES and propagates into the wind medium. The late TeV emission mainly comes from the deceleration of the ES as the FS flux from high latitudes declines rapidly. The decaying index of the early X-ray lightcurve is $\simeq -1.5$, which gives the spectral index of the ES electron spectrum is $p_E \simeq 2.3$ with the closure relation for $\nu_m < \nu_X < \nu_c$. The transition of the X-ray/optical temporal indices from a shallow decay to a steep decay near 10^5 s hints at the occurrence of the jet beak, which implies that the initial half jet opening angle should satisfy

$$\theta_{j,0} \leq 0.03 \left(\frac{E_{K,\text{iso}}}{10^{55} \text{ erg}} \right)^{-1/4} \left(\frac{A_*}{0.5} \right)^{1/4} \left(\frac{t_j}{10^5 \text{ s}} \right)^{1/4} \text{ rad}, \quad (22)$$

where t_j is the jet break time. It further constrains the jet angle to be within $[0.01, 0.03]$ rad, jointly with the discussion of the VLBI observation and the condition for the significant jet lateral spreading discussed above.

The sophisticated behavior of radio afterglows is still challenging in the literature. In our scenario, the early radio bump is the optically thick rising emission of electrons accelerated by the RS. At a late stage, the radio emission becomes dominated by the ES. The radio spectral index at $\sim 2.5 \times 10^6$ s is $\beta \simeq -0.14$ which means that the characteristic synchrotron frequency ν_m has just crossed 5 GHz band (Rhodes et al. 2024), giving $\epsilon_{B,E}^{1/2} \epsilon_{e,E}^2 \leq 6 \times 10^{-5} E_{K,\text{iso},55}^{-1/2}$. With a starting radius of $R_0 \simeq 10^{15}$ cm, $\theta_{j,0} \simeq 0.025$ rad, and a set of parameters shown in Extended Data Table 2 guided by the discussions above, the two-shock scenario could well interpret the multi-wavelength data (Fig. 3). The electron spectra of different regions at several characteristic times are shown in Extended Data Figure 5. Note that the SSC cooling of electrons in the FS has been self-consistently incorporated in the calculation of the electron spectra (Geng et al. 2018). The predicted post-jet-break optical decay is slightly steeper than that observed in our modeling. Nevertheless, the supernova signature only slightly fainter than that of SN 1998bw has been detected beyond $\sim 10^6$ s by both the Pan-STARRS2 Observatory (Fulton et al. 2023) and JWST (Blanchard et al. 2024), and other photometry observations (Kong et al. 2024). Therefore, such discrepancy in late optical lightcurves could be relieved by taking the flux contribution of the supernova into account.

The realistic jet should be structured, however it may be difficult to probe its structure when it is observed on-axis. In our scenario, we adopt the uniform jet approximation to eliminate redundant structure parameters. A reasonable set of parameters could in principle be found to match the observations within the framework of structured jets.

The reverse shock Since the early radio bump is mainly the emission of the RS (Bright et al. 2023), it provides a unique opportunity to probe the characteristics of the RS. In our scenario, the dynamic of the bulk Lorentz factor of the RS could be approximated by a coasting phase during the collision and a decelerating phase with a decaying law of $\propto R^{-g}$ afterwards (Kobayashi & Sari 2000; Zou et al. 2005). The duration of the coasting phase corresponds to the RS crossing time, which is ~ 300 s as indicated by the end of the prompt emission (Axelsson et al. 2024). Therefore, as a simplified but generalized case, we adopt $\Gamma_3 \simeq 200$ (an average value in the fitting of all multi-wavelength data), typical values of $g \simeq 1$ and $\delta_3 \simeq 0.1$, and leave other crucial parameters of the fast shell (i.e., L_f , Γ_f , $\epsilon_{e,3}$, σ_f , and p_3) free, to perform Bayesian posterior searches. The fitting result to the radio bump is shown in Extended Data Figure 6 and Supplementary Table 2. This yields a derived magnetization of 3×10^{-3} for the fast shell, consistent with our modeling for all data. Note that this magnetization applies to the outflow after experiencing energy release in the prompt phase. Therefore, the initial outflow was likely moderately magnetized before dissipation. By leveraging the exquisite radio bump, our analysis constrains the fast shell properties and demonstrates that the original jet had modest but non-negligible magnetization.

DATA AVAILABILITY

Raw VLBA data can be found in the NRAO Data Archive under project code BA161 and TG015. Calibrated data can be obtained upon reasonable request.

CODE AVAILABILITY

The data calibration and imaging using the VLBI pipeline (<https://github.com/SHAO-SKA/vlbi-pipeline.git>) at the China Square Kilometre Array (SKA) Regional Centre. The python code used for calculations in this work can be currently made available upon reasonable request to the corresponding author, and will be public after arrangement soon.

AIPS (<https://www.aips.nrao.edu/index.shtml>)

PARSELTONGUE (<https://github.com/jive-vlbi/ParselTongue>)

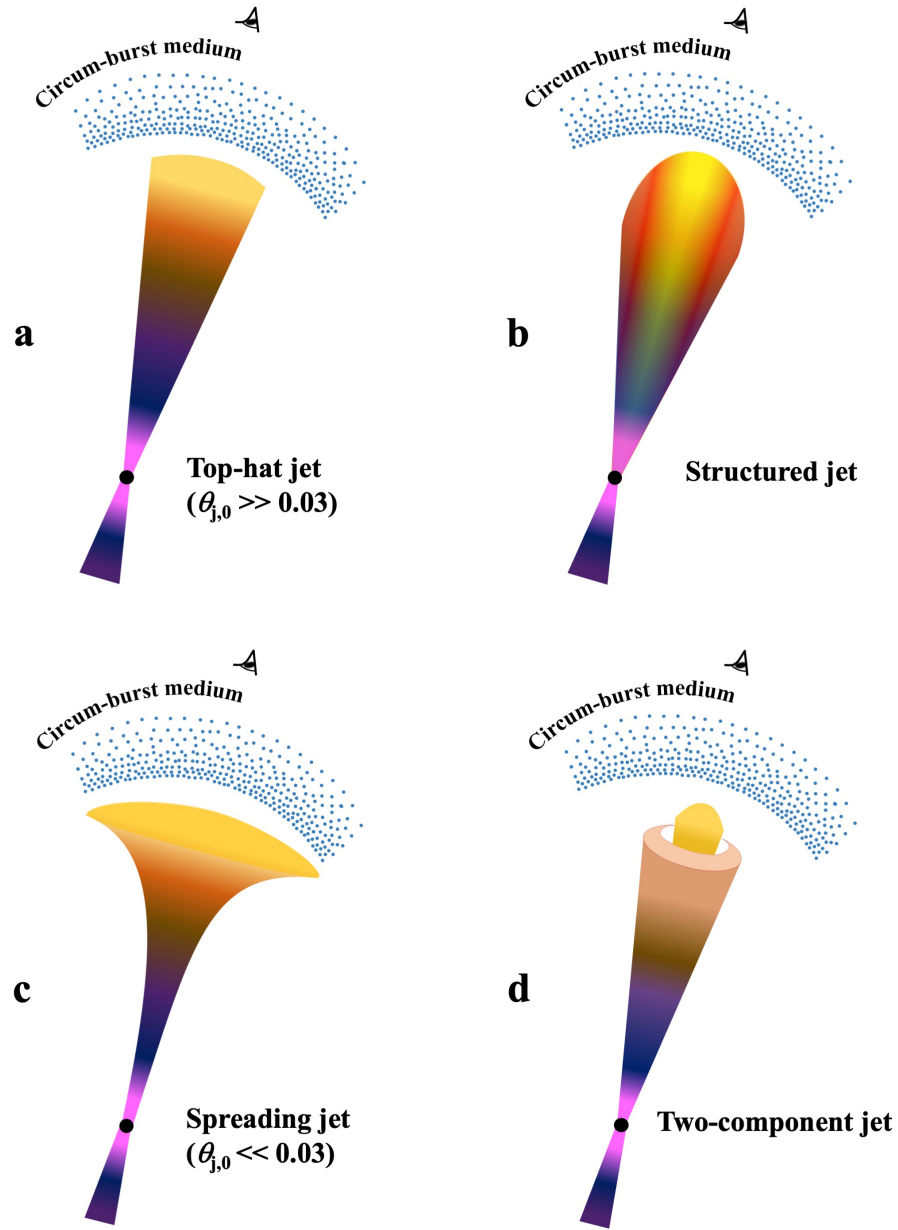
EMCEE (<https://github.com/dfm/emcee>)

This work was supported by the National SKA Program of China (2022SKA0130100, 2020SKA0120300, 2022SKA0120102), the National Natural Science Foundation of China (12321003, 12273113, 12393812, 12393813, 12233002, 12103055, 12041301, 12133007, 12103089), the National Key Research and Development Program of China (2021YFA0718500), the Strategic Priority Research Program of the Chinese Academy of Sciences (XDB0550400), and the International Partnership Program of Chinese Academy of Sciences for Grand Challenges (114332KYSB20210018). JJG acknowledges support from the Youth Innovation Promotion Association (2023331). HXG acknowledges support from Jiangsu Funding Program for Excellent Postdoctoral Talent. BL acknowledges support from the National Astronomical Science Data Center Young Data Scientist Program (NADC2023YDS-04). YL acknowledges support from the Natural Science Foundation of Jiangsu Province (BK20211000). YFH and TA also acknowledge the support from the Xinjiang Tianchi Program.

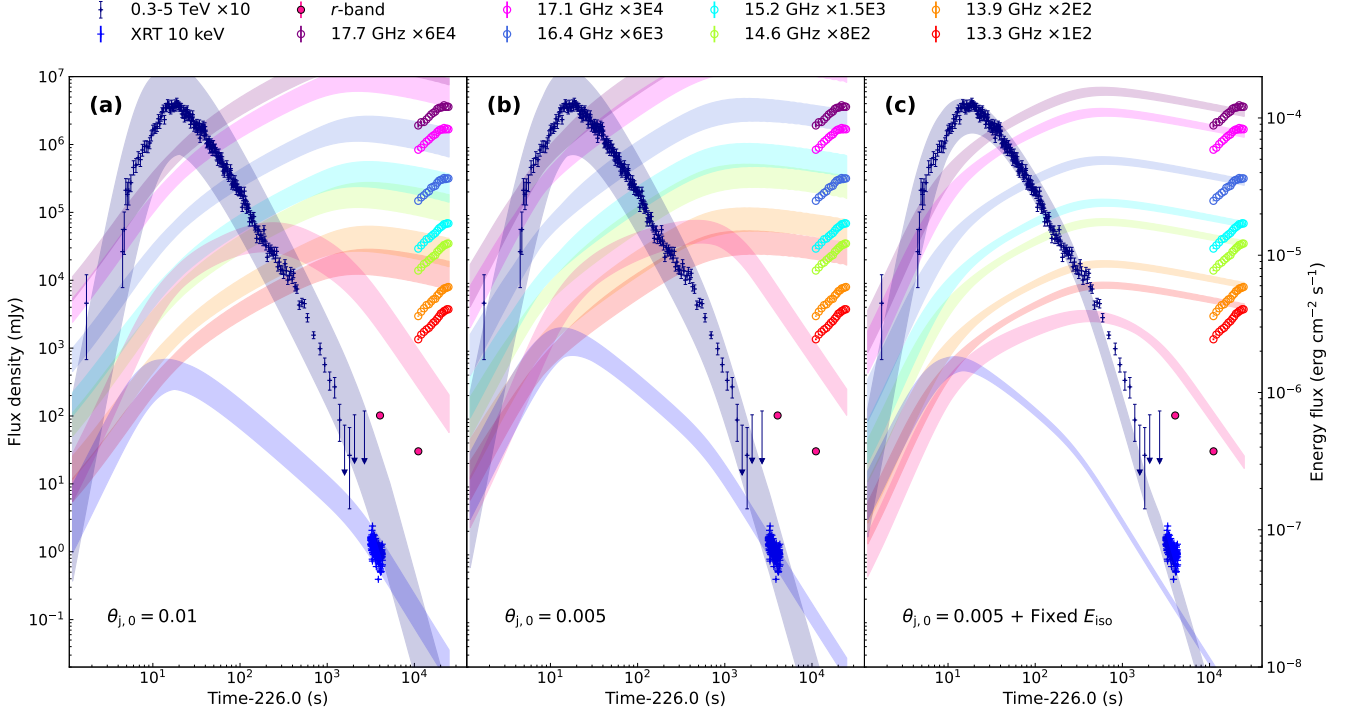
JJG, XFW, TA, BZ, YFH and ZGD wrote the majority of the manuscript; TA, YKZ, ALW and ZJX led the VLBI observation, processed the data, and performed data analyses; YQL and JY participated in VLBI observation and data processing discussions; JJG and HXG developed the numerical code; FX, TRS, and LR collected the multi-wavelength data; JJG, XFW, ZGD, YFH and BZ analysed the results and provided theoretical models; HXG, JR, DX, YL, LL, and YW discussed the results; BL draw the schematic picture of the model; JJG and CRH draw the rest plots. All authors contributed to the analysis and interpretation of the data and to the final version of the manuscript.

The authors declare that they have no competing financial interests.

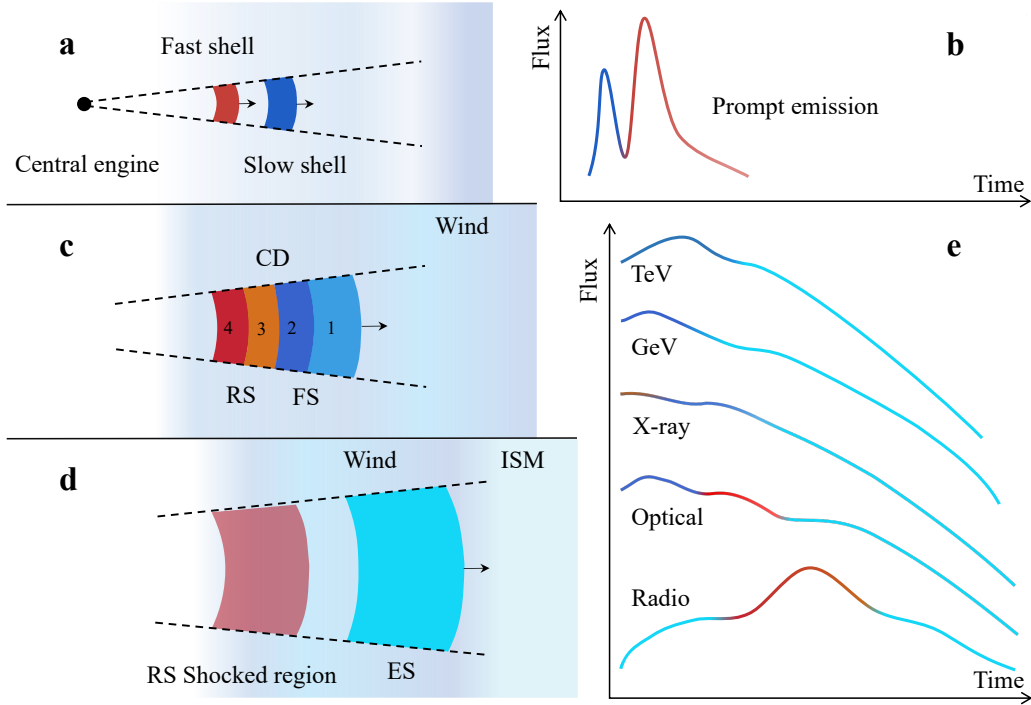
Correspondence and requests for materials should be addressed to T. An, X. F. Wu, Y. F. Huang or Z. G. Dai.



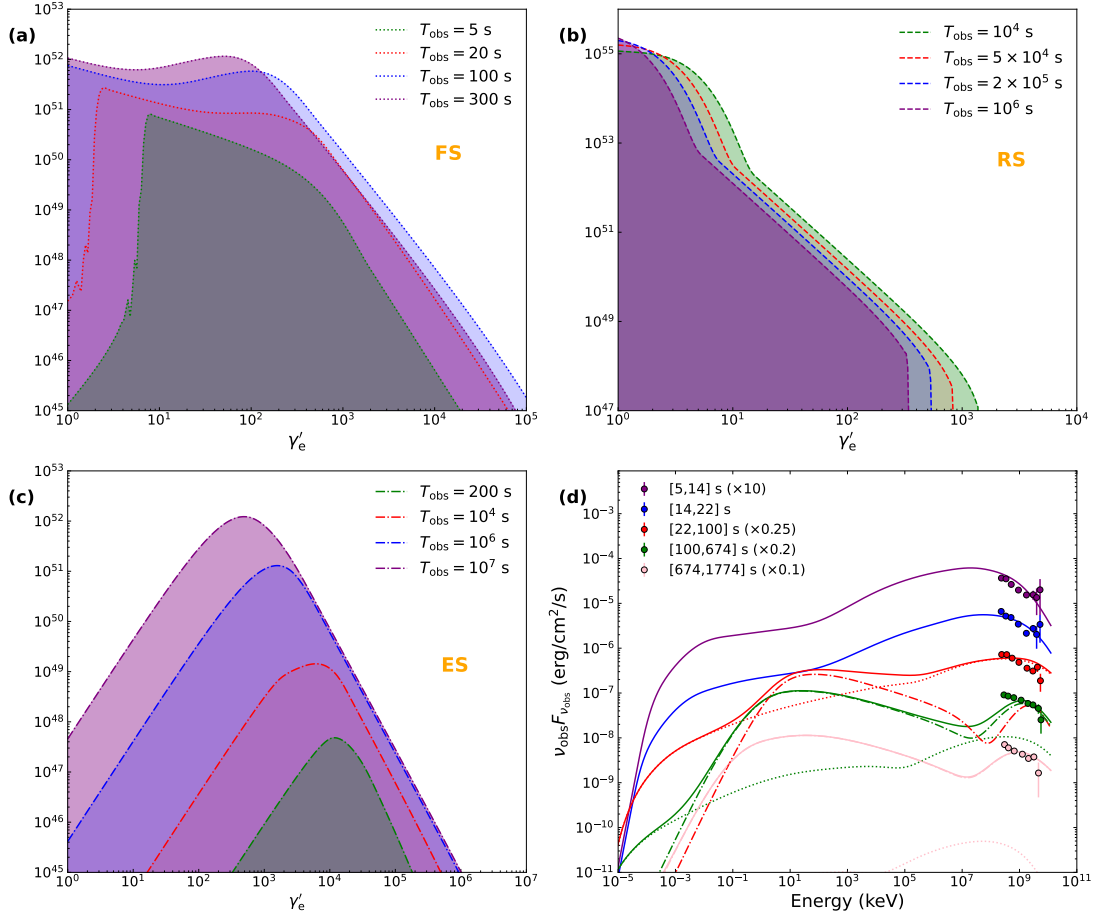
Extended Data Figure 1. A schematic illustration of different scenarios of GRB jets in relativistic phase. In each panel, the eye indicates the on-axis observer. (a) A classical top-hat jet with a uniform distribution of energy and velocity across the jet surface. (b) A prevailing structured jet with the conventional profile. (c) A core-dominated jet spreading at the late stage. (d) A two-component jet with an inner narrow outflow and an outer wide one separated by a hollow region.



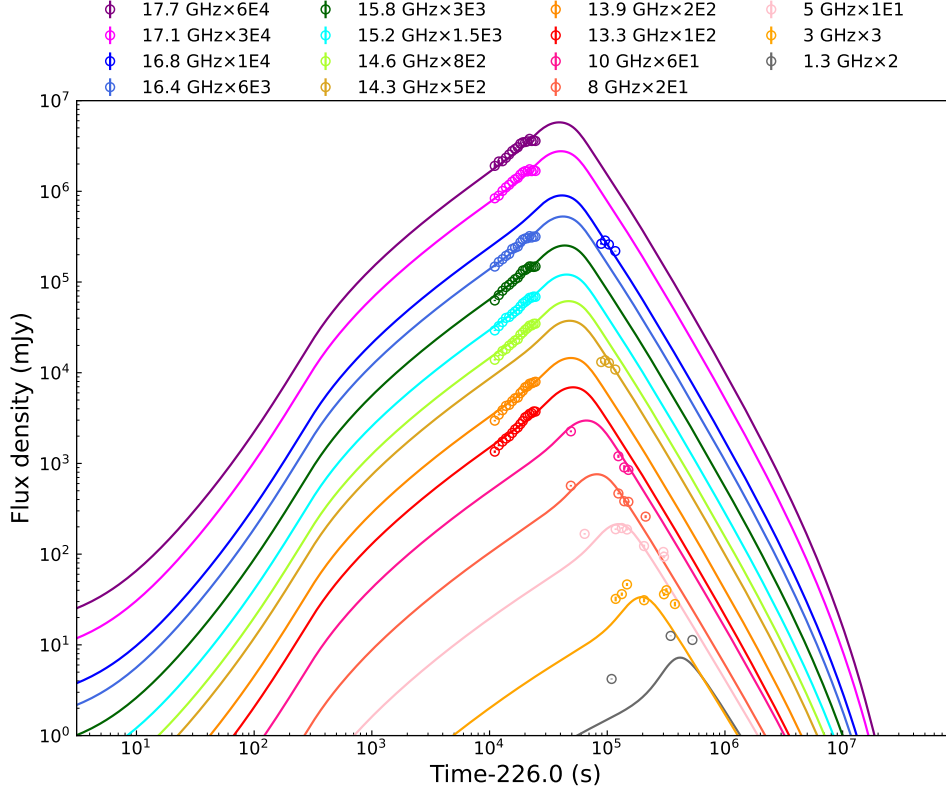
Extended Data Figure 3. The fitting results with external shock model. Each panel shows the fitting results to the data using different strategies. The colored shaded areas correspond to the 3σ confidence regions for lightcurves in different bands with posteriors constrained by the MCMC method (see Supplementary Table 1). (a) Both the TeV lightcurve and spectra (in five time intervals) and the X-ray lightcurve are used in the posteriors search. A conical jet with an initial half-opening angle $\theta_{j,0}$ of 0.01 rad is adopted. (b) Only the TeV information is used in the posteriors search. A narrower jet with $\theta_{j,0} = 0.005$ rad is adopted. (c) Same to (b), but the parameter $E_{K,iso}$ is fixed to a relatively small value (9×10^{54} erg) in order to alleviate the flux excess issue. The corner plots of posteriors in (b) and (c) are shown as Supplementary Figure 1 and Supplementary Figure 2. The flux predicted by the external shock model exceeds the observation data in optical and radio bands significantly in these calculations.



Extended Data Figure 4. The schematic picture of the two-shell collision scenario. Three main epochs of the dynamic evolution and emission of the two-shock system are shown in different panels. (a) Two outflows are launched from the central engine - an early slow shell and a late fast shell. Internal dissipation processes within the shells produce the initial prompt emission (b). (c) The collision between the two shells occurs at $\sim 10^{15}$ cm, producing a forward shock (FS) propagating into materials of the preceding shell, and a reverse shock (RS) propagating into the fast shell, separated by the contact discontinuity (CD). This creates distinct shocked regions labeled with the number “ i ” ($i = 1 - 4$, see Appendix). The short-lived FS contributes to the main peak in TeV lightcurve. (d) After the breakout of the FS into the wind-type interstellar environment, the external shock (ES) is formed. The ES generates the rest part of the TeV lightcurve and the long-lasting X-ray/optical afterglows. The RS detaches from the ES gradually once the injection from the fast shell ceases. The electrons shocked by the RS make brightening bumps in radio frequencies. At late stages, the radio emission is dominated again by the external shock, when the environment becomes a homogeneous interstellar medium. (e) This scenario naturally explains the observed multi-wavelength emissions through the interaction of the shells and subsequent external shocks.



Extended Data Figure 5. Snapshots of the electron and photon spectra. The distribution of electrons shocked by the FS (a), RS (b) and ES (c) at several representative moments in our calculation are shown. Panel (d) shows the spectra at five time intervals by LHAASO. The dotted and dashed-dotted lines are emission from the FS and the ES respectively, and the solid lines are the sum of them.



Extended Data Figure 6. The fitting results of the reverse shock. Our best fitting results to the radio bumps are shown here. The posteriors of reverse shock parameters are listed in Extended Data Table 2, and the corner plot is shown in Extended Data Figure 3.

Extended Data Table 2. Parameters used in modeling the multi-wavelength emission of GRB 221009A.

| Properties of Two Shells | | | | | | | |
|------------------------------------|------------------------|----------------------|----------------------|------------------|------------|----------------|------------|
| L_s | L_f | $E_{\text{iso},s}$ | $E_{\text{iso},f}$ | Γ_s | Γ_f | $\gamma_{p,0}$ | σ_f |
| (erg s ⁻¹) | (erg s ⁻¹) | (erg) | (erg) | | | | |
| 10^{52} | 8×10^{52} | 7.2×10^{54} | 3.2×10^{55} | 65 | 450 | 30 | 10^{-3} |
| Microphysical parameters of the FS | | | | | | | |
| $\epsilon_{e,2}$ | $\epsilon_{B,2}$ | p_2 | δ_2 | η_2^\dagger | | | |
| 0.24 | 1.5×10^{-5} | 2.2 | 0.85 | 1.0 | | | |
| Microphysical parameters of the RS | | | | | | | |
| $\epsilon_{e,3}$ | $\epsilon_{B,3}$ | p_3 | δ_3 | η_3 | | | |
| 0.023 | – | 2.3 | 0.12 | 1.0 | | | |
| Parameters of the ES | | | | | | | |
| $\epsilon_{e,E}$ | $\epsilon_{B,E}$ | p_E | δ_E | η_E | A_* | R_T | |
| 0.019 | 2.2×10^{-4} | 2.4 | 0.75 | 0.1 | 0.1 | 10^{19} | (cm) |

†. η is the fraction of electrons that is assumed to be accelerated by the shock.

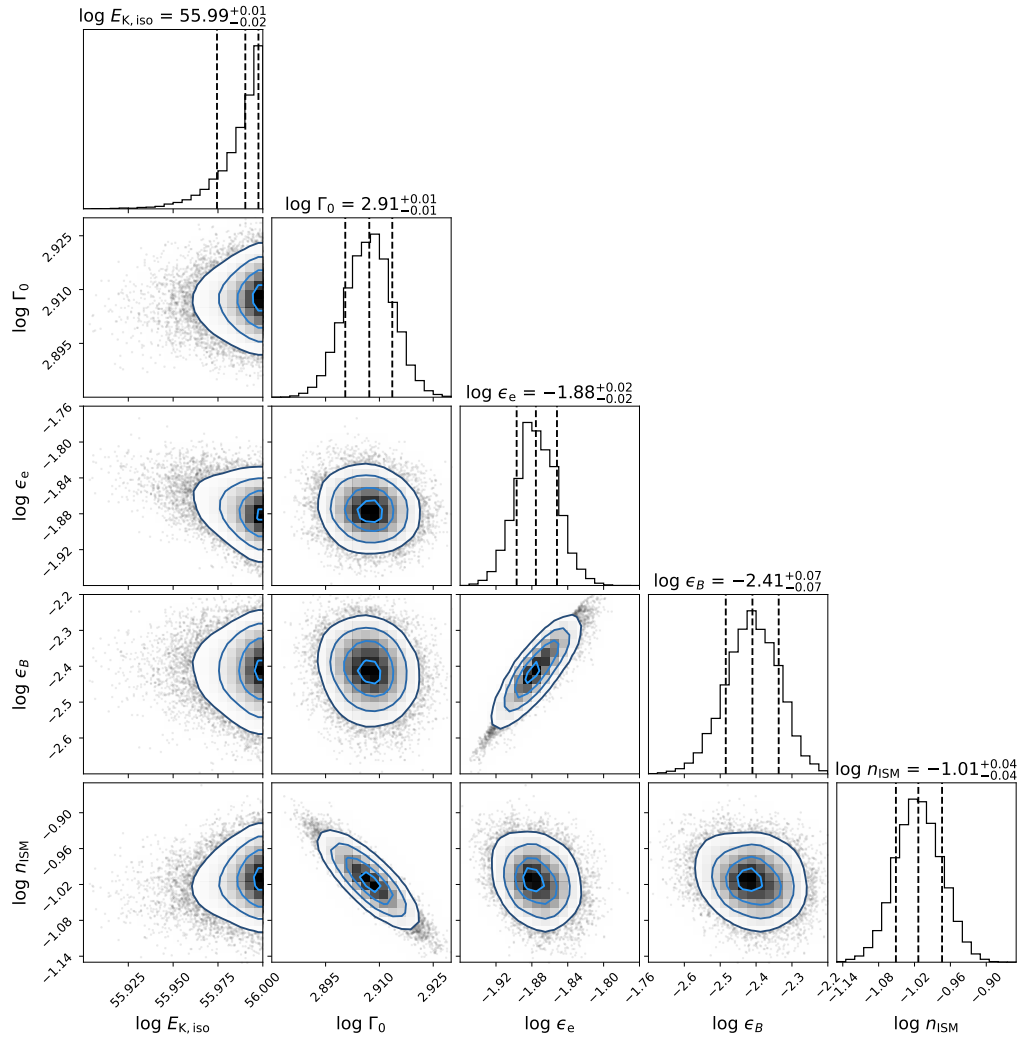
SUPPLEMENTARY MATERIALS

Supplementary Table 1. Posteriors of the external shock parameters.

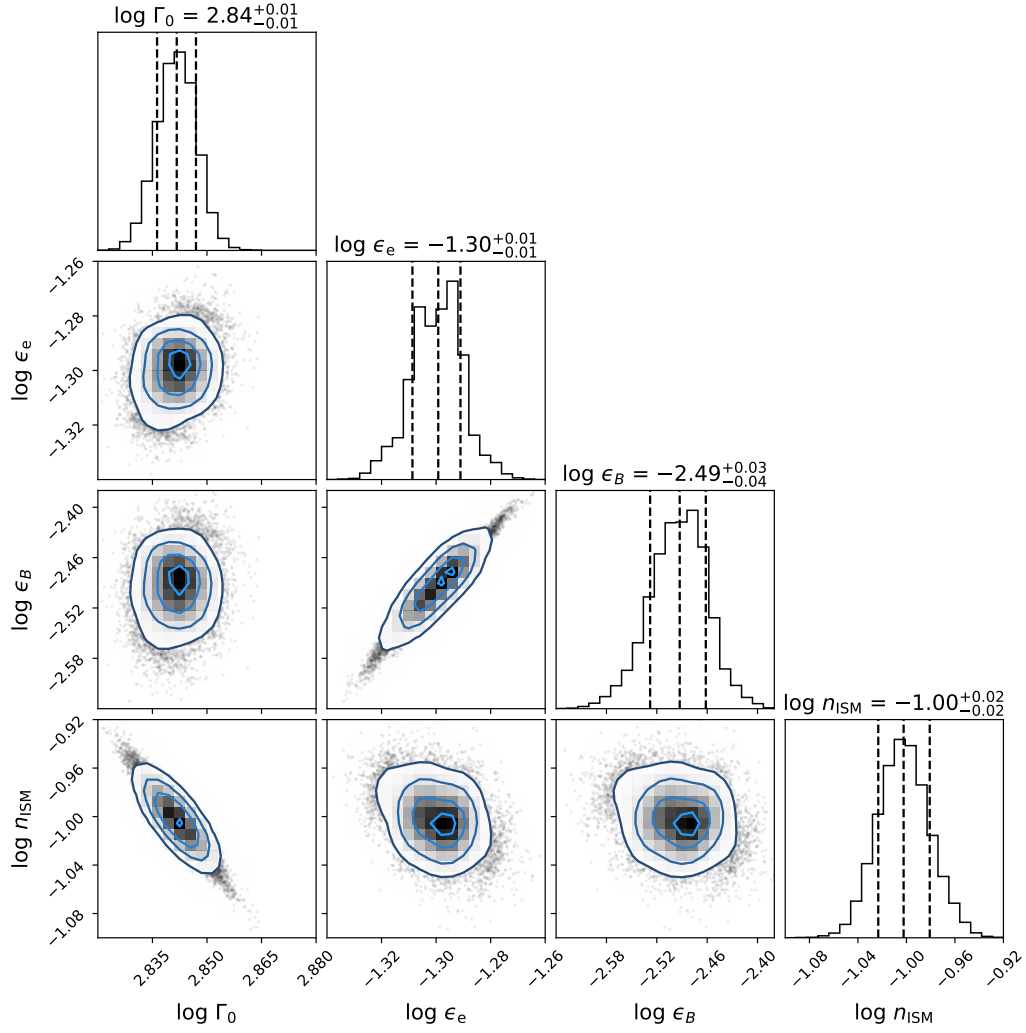
| Case | $\log E_{K,iso}$ (erg) | $\log \Gamma_0$ | $\log \epsilon_e$ | $\log \epsilon_B$ | $\log n_{ISM}$ (cm^{-3}) |
|------|-------------------------|------------------------|-------------------------|-------------------------|-------------------------------------|
| (a) | $55.98^{+0.01}_{-0.03}$ | $2.80^{+0.01}_{-0.01}$ | $-2.14^{+0.03}_{-0.01}$ | $-3.33^{+0.04}_{-0.03}$ | $-0.14^{+0.03}_{-0.04}$ |
| (b) | $55.99^{+0.01}_{-0.02}$ | $2.91^{+0.01}_{-0.01}$ | $-1.88^{+0.02}_{-0.02}$ | $-2.41^{+0.07}_{-0.07}$ | $-1.01^{+0.04}_{-0.04}$ |
| (c) | - | $2.84^{+0.01}_{-0.01}$ | $-1.30^{+0.01}_{-0.01}$ | $-2.49^{+0.03}_{-0.04}$ | $-1.00^{+0.02}_{-0.02}$ |

Supplementary Table 2. Posteriors of the reverse shock parameters.

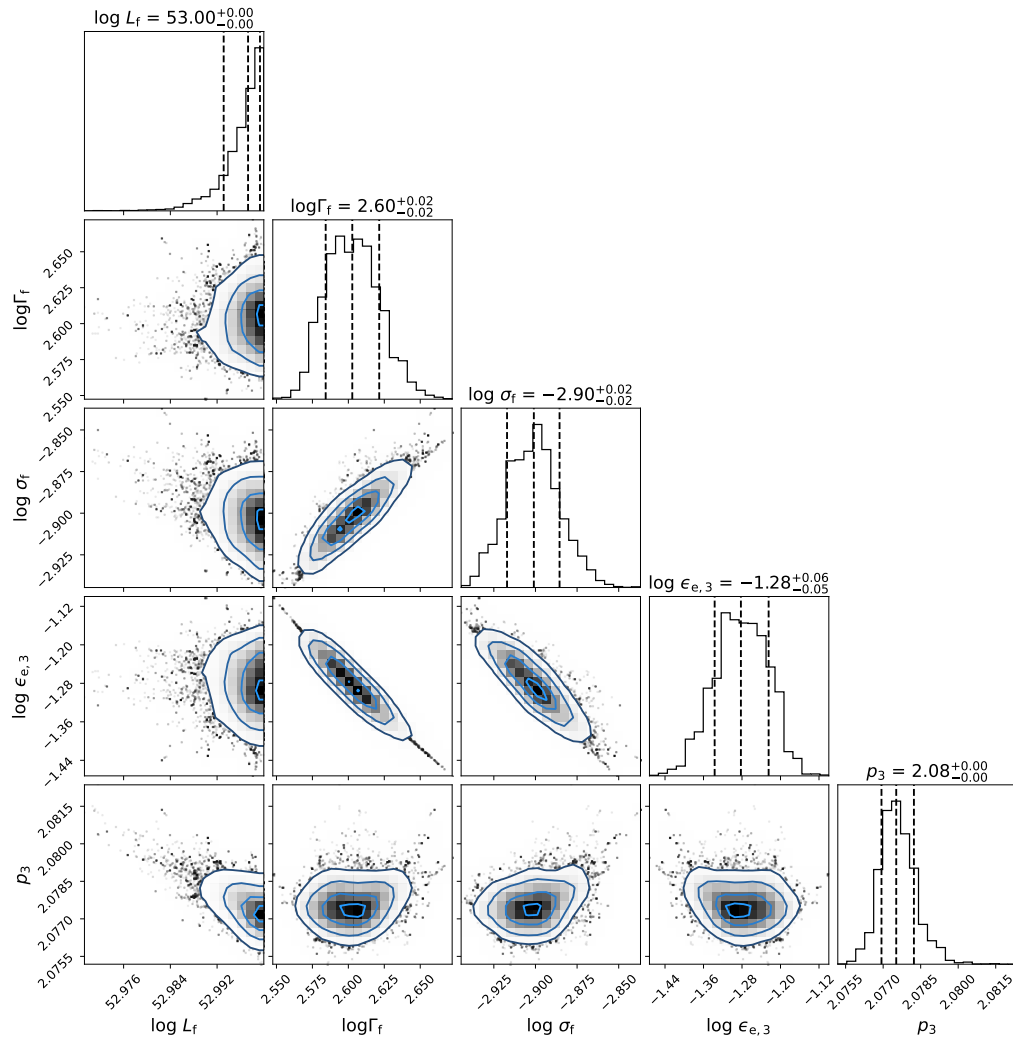
| $\log L_f$ (erg s^{-1}) | $\log \Gamma_f$ | $\log \sigma_f$ | $\log \epsilon_{e,3}$ | p_3 |
|------------------------------------|------------------------|-------------------------|-------------------------|------------------------|
| $53.00^{+0.00}_{-0.00}$ | $2.60^{+0.02}_{-0.02}$ | $-2.90^{+0.02}_{-0.02}$ | $-1.28^{+0.06}_{-0.05}$ | $2.08^{+0.00}_{-0.00}$ |



Supplementary Figure 1. The corner plot of the fitting result of panel (b) in Extended Data Figure 3. The corner plot shows all the one and two-dimensional projections of the posterior probability distributions of the initial isotropic kinetic energy ($E_{K, \text{iso}}$), the initial Lorentz factor (Γ_0), the equipartition parameters for shocked electrons and magnetic field (ϵ_e and ϵ_B), and the circumburst number density (n_{ISM}). The upper limit for priors of $E_{K, \text{iso}}$ is set as 10^{56} erg by assuming that the radiation efficiency should not be less than 10% for such a bright burst. The 1-dimensional histograms are marginal posterior distributions of these parameters. The vertical dashed lines indicate the 16th, 50th, and 84th percentiles of the samples, respectively, which are labeled on the top of each histogram.



Supplementary Figure 2. The corner plot of the fitting result of panel (c) in Extended Data Figure 3. This figure is similar to Supplementary Figure 1 but with $E_{K,\text{iso}}$ fixed to be 9×10^{54} erg (LHAASO Collaboration et al. 2023).



Supplementary Figure 3. The corner plot of the fitting result in Extended Data Figure 6. Note that the marginal posterior distribution of L_f is close to the prior upper limit, but other parameters have converged well.